Optical Materials 161 (2025) 116807

Contents lists available at ScienceDirect

Optical Materials

journal homepage: www.elsevier.com/locate/optmat

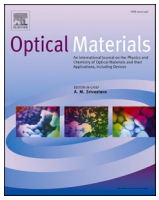

Research Article

Effect of tungsten oxide concentration on structural, morphological, compositional, dispersion energy, and linear/nonlinear optical properties of niobium pentoxide thin films

Panupat Chaiworn [a], Watcharin Teerananattapong [b], Pakpoom Reunchan [b], Auttasit Tubtimtae [c,*], Ekasiddh Wongrat [d,**]

[a] Department of Physics, Faculty of Science and Technology, Chiang Mai Rajabhat University, Chiang Mai, 50300, Thailand
[b] Department of Physics, Faculty of Science, Kasetsart University, Bangkok, 10900, Thailand
[c] Division of Physics, Department of Physical and Material Sciences, Faculty of Liberal Arts and Science, Kasetsart University Kamphaeng Saen Campus, Nakhon Pathom, 73140, Thailand
[d] School of Science, University of Phayao, Phayao, 56000, Thailand

ARTICLE INFO

Keywords:
Niobium pentoxide
Tungsten oxide
Thin films
Spin coating technique
Linear/nonlinear optical properties

ABSTRACT

Metal-oxide semiconductors with tunable optical and electrical properties are essential candidates for the next-generation development of optoelectronic devices. Interestingly, niobium pentoxide (Nb_2O_5) has a high refractive index and wide band-gap semiconductor. The systematically observed modification with property adjustment through controlled doping remains unexplored. In this study, the effect of tungsten oxide (WO_3) incorporation on Nb_2O_5 was first investigated. The Nb_2O_5:WO_3 precursors were consistently mixed at ratios of 90:10, 85:15, and 80:20 and deposited via spin coating on borosilicate glass substrates. X-ray diffraction analysis revealed the peak positions of orthorhombic Nb_2O_5 and monoclinic WO_3 in the patterns. The structural and thermodynamic properties of Nb_2O_5 and WO_3 were studied by DFT calculations, which revealed a strong agreement between the calculated and experimental values, with lattice parameters differing by less than 1.5 % for both materials. Field-emission scanning electron micrographs showed that the surface exhibited a very smooth, dense, and uniform morphology free of cracks and porous nature. In band gap calculation, it was found that the decrease in E_g from 3.84 ± 0.01 to 3.40 ± 0.02 eV with increasing WO_3 concentration can be explained in terms of the occurrence of localized states created between the conduction and valence bands. Standard DFT calculations using the GGA-PBE functional yielded calculated band gaps for Nb_2O_5 (1.84 eV) and WO_3 (1.28 eV), which are significantly lower than the experimental values. A lower transmittance value from ~74 to 67 % as the increasing absorption coefficient value from 0.73×10^3 to 7.00×10^3 cm^{-1} with increasing WO_3 concentration was obtained owing to the higher photon absorption ability in the thin film since the reflectance of the thin film was less than 10 %. The average refractive index values, in the range of 300–1000 nm, increased to 1.629, 1.630, and 1.632 with increasing WO_3 concentration, implying elevated densification or packing density of the thin films with increasing E_U values from 172.58 to 182.28 meV. This imputed the increased localized defect states and demonstrated a strong correlation with the variation in dislocation density. The results from Fourier-transform infrared and micro-Raman spectroscopy revealed that the bonding of the Nb–O–Nb and W–O–W groups and a strong broadband peak corresponded to the O═Nb═O bond. The optical, dispersion energy, optoelectrical, and nonlinear susceptibilities were calculated and investigated for different WO_3 concentrations. The overall increase in average $\chi^{(1)}$ and $\chi^{(3)}$ but decrease in average n_2 values of 0.1316–0.1324, 5.636×10^{-14} to 5.734×10^{-14} esu., and 1.20×10^{-12} to 1.13×10^{-12} esu., respectively, as the energy values at a maximum point of β_c are decreased from 2.78 to 2.48 eV with increasing WO_3 concentration rendered the expansion in the 3D network of the thin films and increase in strength of chemical bonding between the molecules of Nb_2O_5:WO_3, which may be ascribed to a reduction in the E_g value. Photoluminescence was applied to investigate the electronic structure and electron transfer mechanism in the forbidden bandgap of a semiconductor. This study

* Corresponding author.
** Corresponding author.
E-mail addresses: tubtimtae@gmail.com (A. Tubtimtae), Ekasiddhwongrat@gmail.com (E. Wongrat).

https://doi.org/10.1016/j.optmat.2025.116807
Received 14 December 2024; Received in revised form 1 February 2025; Accepted 10 February 2025
Available online 13 February 2025

demonstrates that the synthesized thin films are promising for use in optoelectronics and other technological devices.

1. Introduction

Currently, metal oxide semiconductors (MOSs) have found technological applications because of their propensity to absorb light [1], and transition metal (TM) oxides show remarkable photocatalytic, optoelectronic, electrochemical, chemical sensing, ferroelectricity, energy storage, solar energy conversion, and wave density charging performance [2,3]. These characteristics allow selective oxidation and dehydration of materials with unique physicochemical properties for biomedical applications [4]. Mixed-metal and metal oxides, double-layered metal oxide nanoparticles (NPs), and mixed-metal oxide thin films have been explored for their optical and electrochromic (EC) properties, chromogenic applications, and electrocoagulation of wastewater, such as CuO/ZnO [5], mixed molybdenum–tungsten oxides ($Mo_yW_{1-y}O_{3-\delta}$) [6], WO_3/NiO [3,7], SnO_2/Sb_2O_3 [8], $(MoO_3)_{1-x}(V_2O_5)_x$ [9], and SiO_2/Nb_2O_5 multilayer thin films [10]. In particular, the focus is on metal oxide materials, such as niobium pentoxide (Nb_2O_5) and tungsten oxide (WO_3). Niobium pentoxide (Nb_2O_5), commonly found in niobium oxides, is a high-index n-type semiconductor material with a high refractive index (n = 2–3) [11,12], long-range optical absorption (0.35–7 μm), low corrosion resistance [13], and exceptional thermal and chemical stability [11]. Nb_2O_5 has attracted much attention from academic and engineering research fields because of its rapid growth by the fabrication method, improving its properties for optoelectronic applications [14]. As our background, Nb_2O_5 has various polymorphs, including pseudohexagonal (TT-Nb_2O_5), orthorhombic (T-Nb_2O_5), and monoclinic (B-, M, and H–Nb_2O_5) [15–17]. It is commonly activated in the ultraviolet (UV) region [18]. Previously, Nb_2O_5 thin films were synthesized with a wide energy gap of 2.90–4.60 eV using various methods (e.g., DC/RF magnetron sputtering [19,20], spray pyrolysis [21], chemical vapor deposition [22], ion-assisted electron beam evaporation [23], microwave-assisted hydrothermal synthesis [24], pulsed laser deposition [25], and ion-beam sputtering [26]). However, the properties of Nb_2O_5 films are highly dependent on the deposition method and conditions [27]. Nb_2O_5 has also gained attention in the photonics industry because of its nonlinear optical properties. Thus, it has been extensively used in various technological applications [28,29], optical glasses, and devices [12,19,30] such as waveguides and modulators [31].

To extend Nb_2O_5 absorption to the visible (Vis) range, Nb_2O_5 can be doped with TM cations or nonmetal elements, such as carbon, nitrogen, fluorine, phosphorus, and sulfur, as they can influence and change its structural, optical, electronic, magnetic, photocatalytic, and electrochemical properties [32–35]. Meanwhile, tungsten oxide (WO_3) is an important wide-range spectrum and wide-bandgap semiconductor in the range of 2.84–3.05 eV, featuring wide polymorphism and compositional ratios [36]. WO_3 is one of the most extensively investigated EC materials currently used in electrochromic device (ECD) applications [37] because of its superior transmittance modulation and electrochemical stability. In particular, WO_3 is useful as a transparent cathode in top-emitting organic light-emitting diodes [38], transparent window layers, and flexible organic solar cells [39]. Depending on the growth conditions, different stoichiometries and stable crystalline phases have been found [40]. Thus, different WO_x phases can exhibit remarkable electrical conductance and a highly transparent front window, which is also interesting for industrial applications because it avoids the use of toxic gases during the growth process [41]. However, a previous study reported that mixed-metal oxides perform better than pure oxides and have advanced properties owing to the presence of more than one metal cation in their structure, although one element is richer than another one. These mixed-metal oxides include spinel structures based on 3d TMs that have strong thermal stability, are effective in catalytic reactions, and are used in a wide range of scientific discipline [42].

Various physical and chemical synthesis methods have been used to prepare undoped and doped mixed-TM oxides. For instance, sputtering [3], the dry mixing method [5], solvothermal [6], solid-state reaction processes [8], pulse laser deposition [9], chemical bath deposition [43], physical vapor deposition [44], and hydrothermal methods [45]. Recently, tungsten oxide (WO_3) mixed with nickel oxide (NiO) was synthesized by applying WO_3 concentrations of 10 % and 15 % at a fixed deposition power for radiofrequency (RF) sputtering and temperature. The correlation of the optical and electronic properties with the energy bandgap through WO_3 concentration will be useful for fabricating electrochromic and optoelectronic devices [3].

Among the above synthesis methods, spin coating is a common method that is regarded as a simple process with low cost and low temperature to generate uniform films. This method has become a promising candidate for economical, friendly, energy-saving, and low-pollution technologies for applying thinner films to substrates, accompanied by outstanding application performance in various industrial and technological sectors. The advantage of spin coating over other methods is that it is excellent for both research and quick prototyping to produce very uniform films quickly and easily, which could contribute to improving the quality of thin films as well as the thin and homogeneous coating that can be obtained at varying thicknesses and expanding their application fields. However, the characteristics of the finalized films depend on the inherent properties of the solution, that is, the solution concentration, type of precursor material, pH concentration, solvent nature, and solution temperature. In addition, selected spin process parameters were proposed such as the rotation duration and spin-coating speed [46,47]. Thus, the metal oxide thin films prepared via the chemical solution, which are deposited on a glass substrate using spin coating, can result in high structural, optical, electrical, and electrochemical performances, with an appreciable energy band gap [48]. An understanding of the synthesis parameters required to control the abovementioned performances is crucial for investigation.

Based on the above discussion, there is a lack of in-depth interpretation and understanding of the effect of WO_3 concentration on the thin-film fabrication process. Herein, we synthesized tungsten oxide (WO_3) mixed with niobium pentoxide (Nb_2O_5) thin films with WO_3 concentrations of 10 %, 15 %, and 20 % by fixed spin-coating deposition at room temperature (~25–30 °C).

To the best of our knowledge, the physical properties of spin coated Nb_2O_5:WO_3 films have not been reported previously. Thus, the purpose of this research is to understand the effect of WO_3 concentration in other metal oxides, that is, Nb_2O_5, for the first time, through morphological, structural, dispersion energy, optoelectrical, linear/nonlinear optical parameters, photoluminescence, Raman analysis, and electronic band structure via DFT calculations.

2. Experimental procedure

2.1. Sample preparation

Niobium tungsten oxide (Nb_2O_5:WO_3) thin films were prepared using different indigenous chemical compositions of niobium(V) oxide (99.99 %, Sigma-Aldrich) and tungsten(VI) oxide (99 %, Acros Organics). Nb_2O_5:WO_3 thin films with the ratios of 90:10, 85:15, and 80:20 were prepared by adding 10 %, 15 %, and 20 % WO_3 into 90 %, 85 %, and 80 % Nb_2O_5, respectively. The amounts and concentrations of Nb_2O_5 and WO_3 powder precursors are listed in Table 1. The mixed powder was dissolved in 0.4 g (0.1 M) of ethyl cellulose, 4 mL of

Table 1
The contents of material preparation for Nb_2O_5:WO_3 ratios.

Ratio	Nb_2O_5		WO_3 (g)	
	Gram (g)	Molar (M)	Gram (g)	Molar (M)
90:10	0.90	0.38	0.10	0.05
85:15	0.85	0.36	0.15	0.07
80:20	0.80	0.33	0.20	0.10

α-terpineol, and 5 mL of ethanol (The ratio of α-terpineol:ethanol is 1:1.25). The solution was then stirred vigorously for 90 min until it became a homogeneous white solution. Borosilicate glass substrates were cut with a dimension of 2.5 × 2.5 cm^2, cleaned with acetone, methanol, and deionized (DI) water under an ultrasonic cleaner for 10 min each, and dried on a hot plate at 100 °C. A well-cleaned glass substrate was placed on a spin coater, and a few drops of the mixed Nb_2O_5 and WO_3 solution were dropped. A TCH-EZ4 programmable spin coater was operated at 2000 rpm for 15 s. A Nb_2O_5:WO_3 thin film with each compositional ratio was coated twice and then calcined at 450 °C for 1 h. The Nb_2O_5:WO_3 thin films with ratios of 90:10, 85:15, and 80:20 are shown in Fig. 1.

2.2. Investigation of morphological, structural, and optical characteristics

The surface morphologies of the films were investigated using an ultrahigh-resolution scanning electron microscope (UHR-SEM, TESCAN CLARA) equipped with an energy dispersive X-ray spectroscope (EDS, Oxford Ultim Max) with a detector size of 40 mm^2 to determine the chemical composition of the thin films. The surface topography of the Nb_2O_5:WO_3 thin films at each ratio was investigated using nGauge atomic force microscopy (AFM, ICSPI). The structural characteristics of the Nb_2O_5:WO_3 thin films were characterized using an X-ray diffractometer (XRD; Rigaku, Model: SmartLab, $\lambda_{Cu\text{-}K\alpha}$ = 1.544 Å, 40 kV, and 30 mA) under grazing incidence conditions with 2θ of 10°–80°. Micro-Raman spectroscopy was implemented using a triple monochromator, and the spectra were recorded using a frequency-doubled green Nd:YVO_4-based diode-pumped solid-state laser at an excitation wavelength of 532 nm, operating at 150 mW in the wavenumber range of 50–1500 cm^{-1} to identify the groups of elemental composition (Thermo Fisher Scientific, DXR SmartRaman). Fourier-transform infrared (FT-IR) spectroscopy was also performed using PerkinElmer Scientific (Spectrum Two FT-IR spectrometer) in the 400–2000 cm^{-1} range. The fluorescence spectra were recorded using a spectrofluorometer (Jasco, FP-8500) with a xenon lamp as the excitation source (λ_{ex} = 255 nm). Finally, a UV–Vis–NIR spectrometer (Varian Cary 50 Conc.) was used to observe the transmittance and reflectance spectra of the Nb_2O_5:WO_3 thin films in the spectral range of 300–1100 nm.

2.3. Computational details

To investigate the structural and electronic properties of semiconductor materials in the form of thin films or monolayers, previously, first principle calculations with the plane wave pseudopotential method implemented in the Quantum ESPRESSO distribution were used; for example, Mn chalcogens in the two structural phases (H and T) of MnX_2 monolayers [49]. In this study, for Nb_2O_5 and WO_3, DFT calculations were implemented in the Vienna *ab initio* simulation package [50,51] within the generalized-gradient approximation (GGA) proposed by Perdew, Burke, and Ernzerhof (PBE) [52]. To describe the ionic-core-valence electron interactions, we adopted projector-augmented wave potentials with 12, 5, and 6 valence electrons for Nb ($4d^4 5s^1$), W ($5d^4 6s^2$), and O ($2s^2 2p$), respectively. For Nb_2O_5, we adopted an orthorhombic crystal structure with the space group *Pbam*. For WO_3, we adopted a monoclinic crystal structure with a space group *2/m*. The crystal structures were previously observed experimentally and were consistent with the XRD spectroscopy results.

A primitive cell of Nb_2O_5 comprises 16 Nb and 42 O atoms, following the atomic coordinates and disordered orthorhombic crystal structure (TT-phase) proposed in a previous study [53]. Note that although this TT-phase of Nb_2O_5 was proposed to be a defective, nonstoichiometric structure, we still use the Nb_2O_5 notation for this material for simplicity and to be consistent with all the results here. For the Brillouin zone integration, 4 × 1 × 6 and 3 × 3 × 3 special Monkhorst–Pack k-point meshes were used for Nb_2O_5 and WO_3, respectively. The energy cutoff for plane-wave expansion was set to 520 eV. To simulate W-doped Nb_2O_5, we adopted the supercell approach, in which a 2 × 1 × 2 repetition of the primitive cell is used to construct the supercell. All the atoms were relaxed until the residual forces were less than 0.02 eV/Å.

3. Results and discussion

3.1. Structural study

Fig. 2 shows the XRD patterns of Nb_2O_5:WO_3 at ratios of 90:10, 85:15, and 80:20. The peak positions for orthorhombic Nb_2O_5 are located at 2θ = 22.6°, 28.3°, 28.8°, 36.6°, 37.1°, and 46.1°, corresponding to the (001), (180), (200), (181), (211), and (002) planes, respectively (JCPDS no. 027–1003). Meanwhile, the peak positions for monoclinic WO_3 are located at 2θ = 23.6°, 24.4°, 33.2°, 34.2°, and 39.7°, corresponding to the (020), (200), (022), (202), and (131) planes,

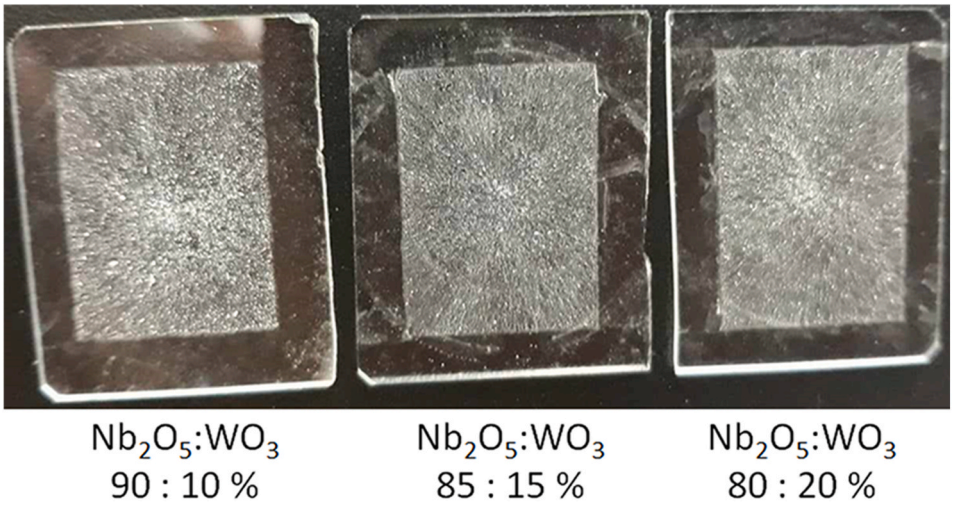

Fig. 1. Photographs of Nb_2O_5:WO_3 in each ratio concentration.

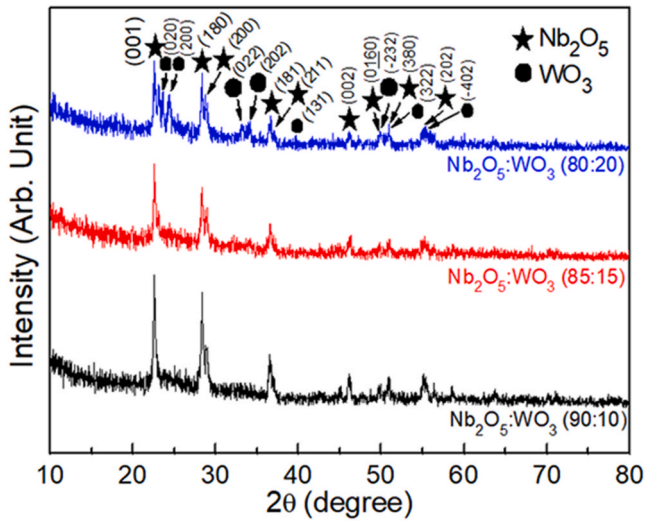

Fig. 2. XRD patterns of Nb_2O_5:WO_3 thin films with ratios of 90:10, 85:15, and 80:20.

respectively (JCPDS no. 043–1035). The overlapped peak positions for Nb_2O_5 and WO_3 are observed at 2θ = 49.8°, 50.9°, and 55.3° with the (0160)/(−232), (380)/(322), and (202)/(−402) planes for Nb_2O_5/WO_3, respectively. Furthermore, slightly decreasing intensities of the main diffraction peaks of Nb_2O_5 at 22.6°, 28.3°, 28.8°, and 36.6° are observed with increasing WO_3 concentration. This occurrence is due to the addition of WO_3 into the Nb_2O_5 lattice, which may weaken the long-range ordered Nb–O bonds and hinders the crystalline to amorphous modification of the thin film, similar to J. Vivekanandan et al. [3]. Increasing the WO_3 concentration in the Nb_2O_5 lattice achieves structural modification from crystalline to amorphous, which has an advantage in the ion diffusion pathway in the thin film for practical electro-optical devices [3,54].

Fig. 3 illustrates the crystal structures of Nb_2O_5 and WO_3 obtained via DFT calculations within the GGA-PBE functional. Panel (a) shows the structure of Nb_2O_5, characterized by distorted NbO_6 octahedra forming a layered arrangement along the b-axis with lattice dimensions of a = 6.202 Å, b = 30.071 Å, and c = 3.860 Å. The elongated b-axis reflects the complex stacking of the NbO_6 units. Panel (b) depicts the WO_3 structure, comprising nearly regular WO_6 octahedra in a 3D network with lattice parameters of a = 7.729 Å, b = 7.841 Å, and c = 7.535 Å. This

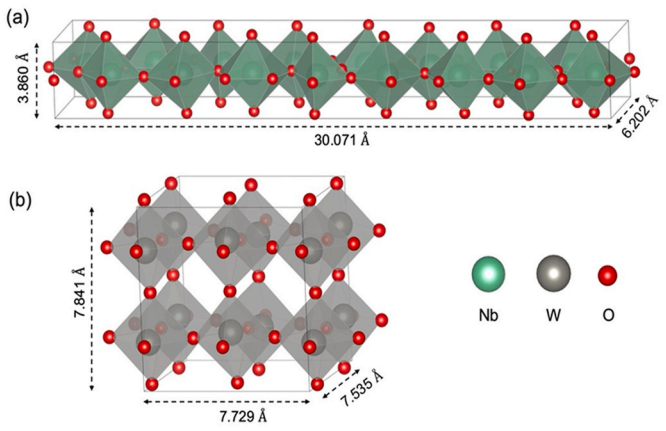

Fig. 3. Simulated crystal structures of (a) Nb_2O_5 and (b) WO_3 via DFT. The structures are visualized with polyhedra representing NbO_6 and WO_6 octahedra, where Nb atoms are in gray, W atoms in green, and O atoms in red. (For interpretation of the references to colour in this figure legend, the reader is referred to the Web version of this article.)

arrangement highlights the structural differences between the two materials, emphasizing the anisotropic nature of Nb_2O_5 and the relatively symmetric framework of WO_3. The red spheres represent oxygen atoms, whereas the gray and green spheres correspond to Nb and W atoms, respectively.

Tables 2 and 3 compare the structural and thermodynamic properties of Nb_2O_5 and WO_3 obtained from DFT calculations using the GGA-PBE functional and the experimental data. The results show a strong agreement between the calculated and experimental values, with the lattice parameters differing by less than 1.5 % for both materials. This demonstrates the accuracy of the computational approach for capturing the structural features of these oxides. For thermodynamic stability, the calculated formation enthalpies (ΔH_f) deviated from the experimental values by only 1.85 % for Nb_2O_5 and 0.34 % for WO_3. These results validate the reliability of the GGA-PBE functional for accurately modeling the structural and thermodynamic properties of metal oxides in this work.

3.2. Morphological characteristics and compositional analysis

FESEM micrographs of Nb_2O_5:WO_3 at ratios of 90:10, 85:15, and 80:20 are shown in Fig. 4(a–c), respectively. The surface has a very smooth, dense, and uniform morphology, free of cracks and a porous nature. This is evidenced by the fact that increasing the WO_3 concentration does not change the overall thin-film morphology, and the films are still homogeneous and tightly packed on the glass substrate. However, notably, some crystal grains or residuals increase and the thickness of the film, as shown in Fig. 4(d–f), is reduced from 2.40 m to 0.40 μm with increasing WO_3 concentration. This can be explained by the fact that as the WO_3 concentration increased, more distribution effect and roughness of the thin film are observed, leading to more crystal grains, residuals, and lower thickness of the films.

Fig. 5(a–c) shows 3D AFM images of the Nb_2O_5:WO_3 thin films at ratios of 90:10, 85:15, and 80:20 in a scanning area of 10.2 × 10.2 μm^2. According to the AFM results, the root mean square roughness values are calculated to be 7.94, 54.46, and 92.70 nm with increasing WO_3 concentration. Thus, with increasing WO_3 concentration, the topology of the surface roughness of the thin film changed and becames higher, which is consistent with the FESEM micrographs.

The compositional analysis of Nb_2O_5:WO_3 with different ratios was conducted using EDS. The spectra with altered weight percentages of Nb, O, and W elements are shown in Fig. 6(a1–c1). As detailed in the EDS results, niobium, oxygen, and tungsten were found in the synthesized Nb_2O_5:WO_3 thin films and no additional elements were found in the spectra, confirming the purity of the thin films. According to the pie chart of atomic percentages of elements in Fig. 6(a2–c2), when tungsten oxide was added from 10 % to 20 % in niobium pentoxide, the tungsten (W) content increased as the niobium (Nb) content decreased, which is the same as the weight percentage. Consequently, the oxygen content increased with increasing WO_3 concentration because oxygen is incorporated by niobium and tungsten [3].

3.3. Optical properties

The optical transmittance (T) spectra of the Nb_2O_5:WO_3 thin films with ratios of 90:10, 85:15, and 80:20 are displayed in Fig. 7(a). The

Table 2
Comparison of lattice parameters, angles (α, β, γ), and formation enthalpies (ΔH_f) for Nb_2O_5 obtained from DFT calculations using the GGA-PBE functional and experimental data.

Properties	GGA-PBE	Experiment
a, (Å), b (Å), c (Å)	6.202, 30.071, 3.860	6.168, 29.312, 3.936
α (°), β (°), γ (°)	90.00, 90.00, 90.00	90.00, 90.00, 90.00
ΔH_f (eV/f.u.)	−19.63	−20.00 [61]

Table 3
Comparison of lattice parameters, angles (α, β, and γ), and formation enthalpies (ΔH_f) for WO_3 obtained from DFT calculations using the GGA-PBE functional and experimental data.

Properties	GGA-PBE	Experiment
a, (Å), *b* (Å), *c* (Å)	7.535, 7.729, 7.841	7.297, 7.539, 7.688
α (°), β (°), γ (°)	90.00, 90.15, 90.00	90.00, 90.00, 90.00
ΔH_f (eV/f.u.)	−8.72	−8.75 [61]

transmittance spectra for each ratio of Nb_2O_5:WO_3 thin films showed the high average transmittance percentage values in the wavelength range of 400–1100 nm. The highest average transmittance of ~74 % was obtained for the Nb_2O_5:WO_3 (90:10) thin film. Decreased transmittance values of ~69 and 67 % are observed for Nb_2O_5:WO_3 85:15 and 80:20, respectively. Notably, the higher the WO_3 concentration, the lower the optical transparency and the lower the thickness of the thin film. This is explained by the fact that a lower thickness leads to more residuals, high-density natural defects, and surface roughness, which is attributed to a greater light scattering effect, indicating a lower crystalline quality in the synthesized thin film. A low transmittance of 42 % was also observed in the graphene doped Nb_2O_5 layer [55]. However, high transmittance in the visible to near-infrared (NIR) region is important for applications in smart windows, solar cells, and monitors [56]. A dramatically reduced transmittance was observed in the wavelength range of 300–400 nm owing to fundamental absorption, which was attributed to the transfer of electrons from O^{2-} to Nb [57,58].

Meanwhile, the optical reflectance (*R*) spectra are displayed in Fig. 7 (b). The spectrum of each thin film showed a similar characteristic of increasing as a function of the wavelength. A fluctuation or wave-like pattern in the reflectance spectra is caused by the interference of light reflected from the air–film and film–glass interfaces [59]. The average *R* values for each thin film are less than 10 %, indicating that the absorption and transmission characteristics of the thin films are the main effects, and these low reflectance values make our synthesized thin films important for anti-reflection applications [60]. Moreover, the reflectance characteristics of the thin films had a minor effect, and the *R* values are not much difference.

The absorption coefficient (α) was calculated from the transmittance and reflectance spectra using the thin film thickness in accordance with the subsequent relation, as expressed in Eq. (1) [61]:

$$\alpha = \frac{1}{t} ln\left[\frac{(1-R)^2}{T}\right], \quad (1)$$

where *t* is the thickness of the Nb_2O_5:WO_3 thin film and *T* and *R* are the transmittance and reflectance, respectively. Fig. 7(c) shows the trend of the absorption coefficients of the different Nb_2O_5:WO_3 thin films. The spectra are almost identical and increased over the entire wavelength range (300–1100 nm). The average α values are 0.73×10^3, 1.82×10^3, and 7.00×10^3 cm^{-1} for the Nb_2O_5:WO_3 (90:10), Nb_2O_5:WO_3 (85:15), and Nb_2O_5:WO_3 (80:20) thin films, respectively. Owing to the lower transmittance with increasing WO_3 concentration, an increasing α value was obtained by the higher photon absorption ability in the thin film as the reflectance of the thin film is less than 10 %.

Then, the α values were added in the conventional Tauc relation, as shown in Eq. (2) for energy bandgap or direct bandgap evaluation [48,62]:

$$\alpha h\nu = A\left(h\nu - E_g\right)^{1/2}, \quad (2)$$

where $h\nu$ is the photon energy, E_g is the energy band gap or direct band gap, and *A* is a constant. The slope of the fitting gives the degree of disorder value and is called the Tauc parameter (A^2) [63]. In Fig. 7(d), the intercept of the extrapolating tangent line on the x-axis at $(\alpha h\nu)^2 = 0$ can be evaluated. The calculated E_g values for the Nb_2O_5:WO_3 (90:10), Nb_2O_5:WO_3 (85:15), and Nb_2O_5:WO_3 (80:20) thin films are 3.84 ± 0.01, 3.75 ± 0.01, and 3.40 ± 0.02 eV, while A^2 values are equal $(123 \pm 6) \times 10^{12}$, $(107 \pm 5) \times 10^{12}$, and $(64 \pm 3) \times 10^{12}$ eV/cm^2, respectively. The decrease in A^2 values indicated higher structural disorder in thin films due to more homopolar bond formation at the Nb_2O_5 and WO_3 interfaces, which agrees with the literature of Ref. [63]. Meanwhile, the

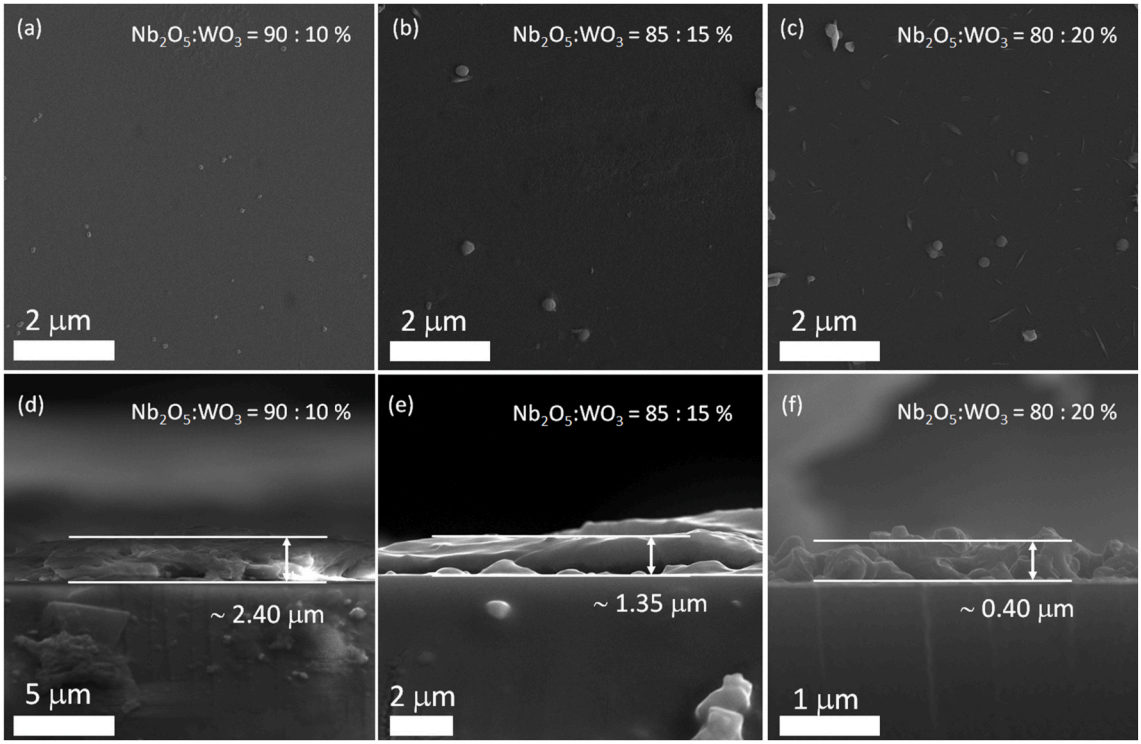

Fig. 4. Surface characteristics and cross-sectional images of Nb_2O_5:WO_3 thin films (a, d) 90:10, (b, e) 85:15, and (c, f) 80:20.

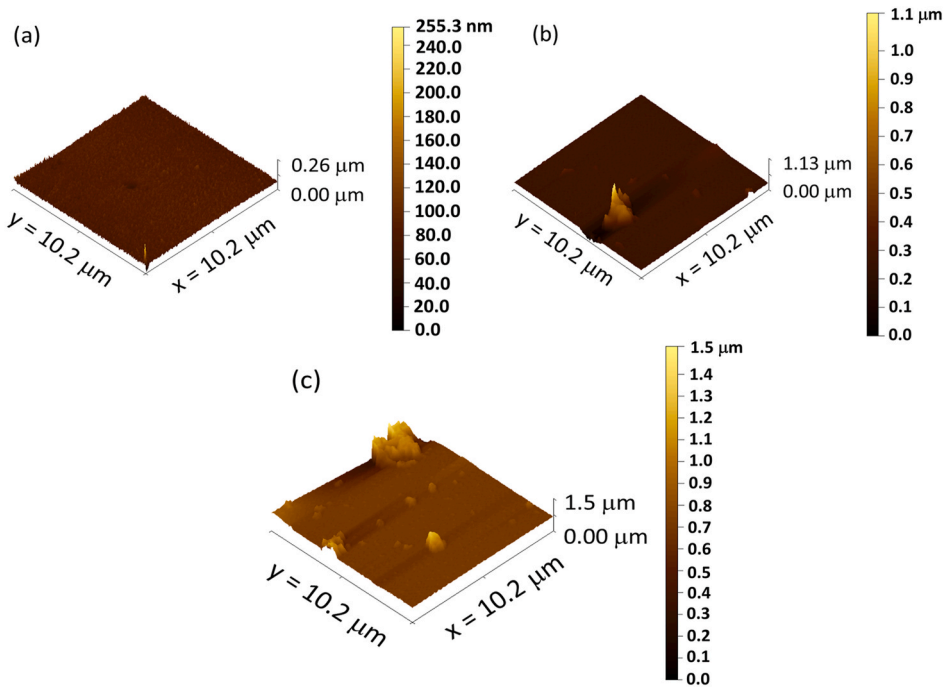

Fig. 5. 3D AFM images of Nb_2O_5:WO_3 thin films with ratios of (a) 90:10, (b) 85:15, and (c) 80:20.

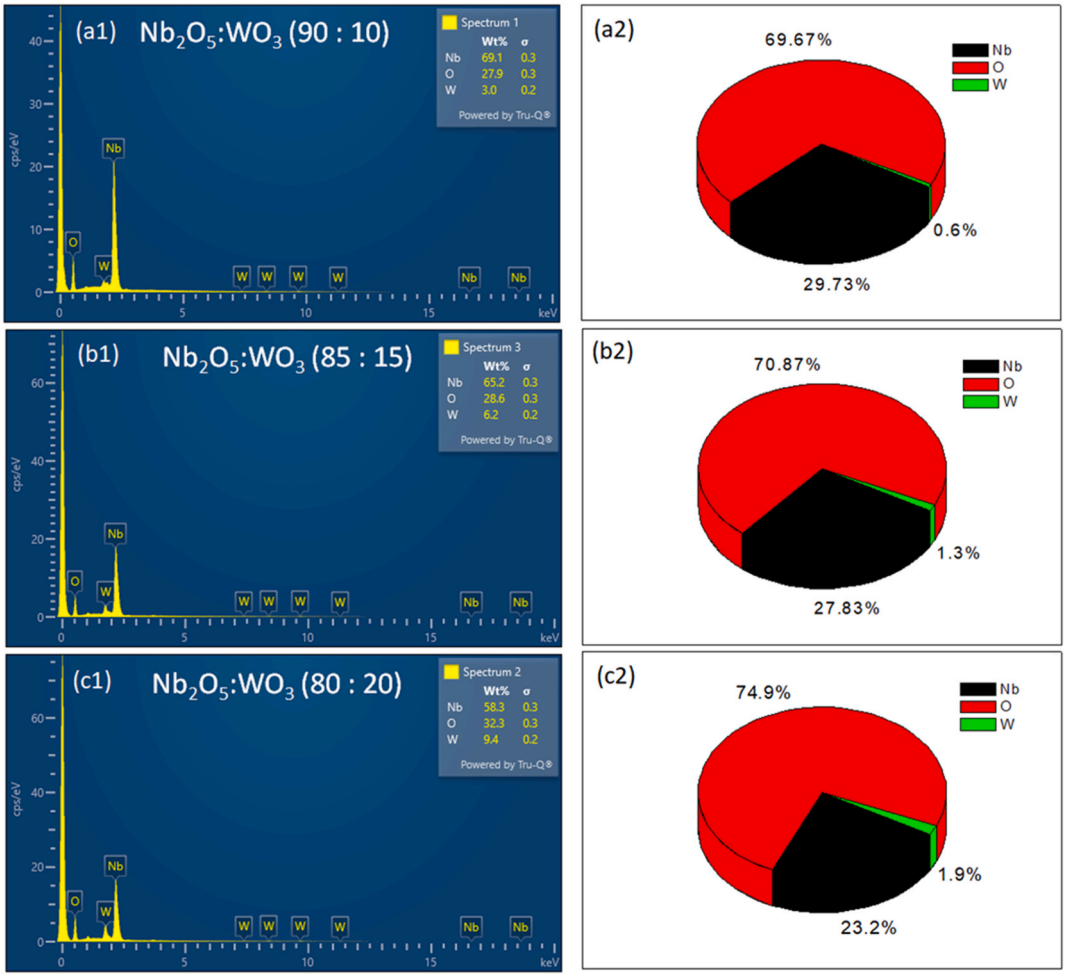

Fig. 6. (a1–c1) EDS spectra and (a2–c2) atomic percentages of Nb_2O_5:WO_3 thin films with ratios of 90:10, 85:15, and 80:20.

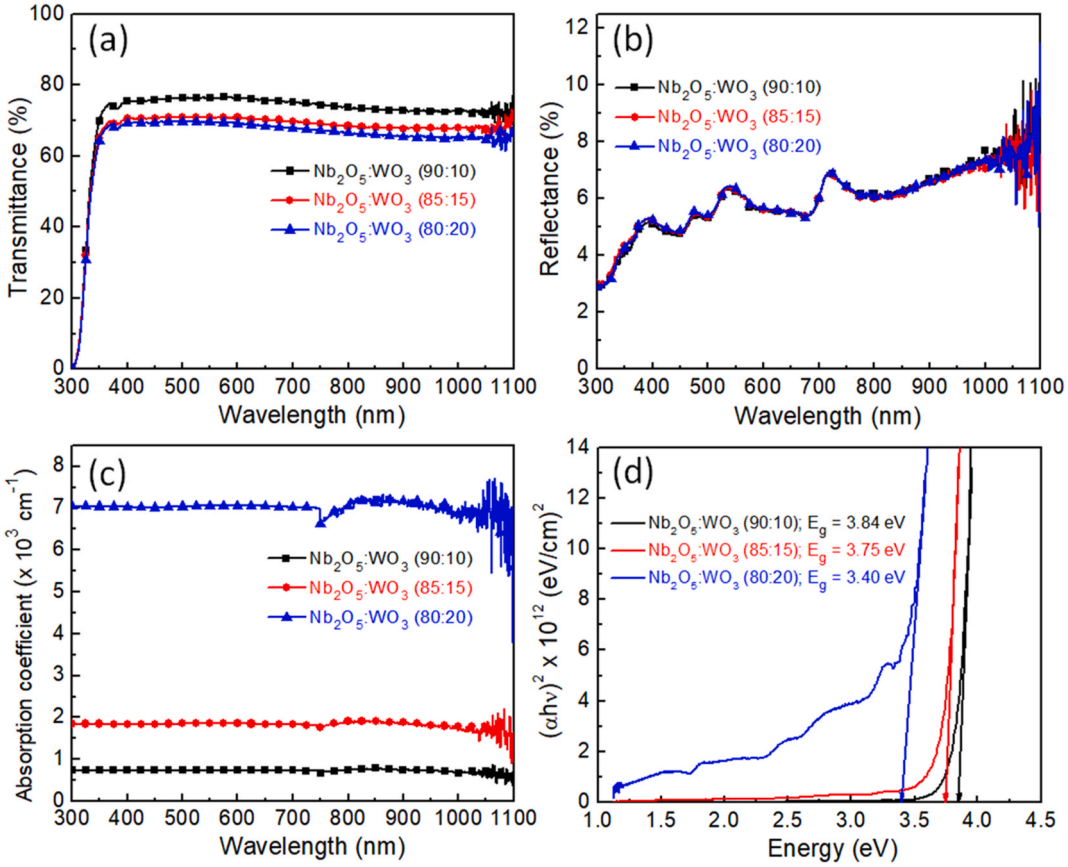

Fig. 7. (a) Optical transmittance, (b) reflectance, (c) absorption coefficient, and (d) Tauc plot analysis for E_g determining Nb_2O_5:WO_3 thin films with ratios of 90:10, 85:15, and 80:20.

decrease in E_g can be explained in terms of the occurrence of localized states created between the conduction band (CB) and valence band (VB) [62,64]. This is similar to J. Vivekanandan et al., who explained that the major transition arises at the near band edge (NBE) between the CB and VB for p-type MOSs, and other transitions with the decrease in E_g values but higher compared to the theoretical direct band gap value of WO_3 (E_g = 2.56 eV) [65] and Nb_2O_5 (E_g = 3.49 eV) [66] also occur as the increase in dopant amount owing to the generated intraband defect, crystalline imperfections, and carrier impurities, including metal deficiency or oxygen access, resulting in a shift in the absorption edge towards the higher wavelength of the incident photons [3,67]. Furthermore, the alteration of E_g values may depend on many factors, such as the coating speed (rpm), granular structure, grain boundary, and the nature and concentration of precursors [48].

A schematic illustrating the mechanism of decreasing E_g values with increasing WO_3 concentration is illustrated in Fig. 8. More generated localized states were formed in the forbidden band gap and were located near the CB owing to the donor dopant WO_3. This causes the Fermi level to move closer to the CB, which is attributed to the decreasing energy band gap or direct band gap. Thus, the low energetic bound conduction electrons can be effortlessly transferred from these localized states to the CB, leading to higher electron mobility. Notably, WO_3 concentration can modify the optical properties, making thin films promising for opto-electronics and electrochromic applications [3].

Fig. 9 presents the electronic band structures of Nb_2O_5 and WO_3 calculated using DFT. For Nb_2O_5 (Fig. 9(a)), the computed indirect band gap is (E_g = 1.84 eV), whereas WO_3 (Fig. 9(b)) exhibits a direct band gap of (E_g = 1.28 eV) at the Γ-point. The wider band gap of Nb_2O_5 makes it suitable for applications such as dielectric layers and wide bandgap semiconductors. In contrast, the direct band gap of WO_3 enables efficient absorption of visible light, making it well suited for photocatalytic

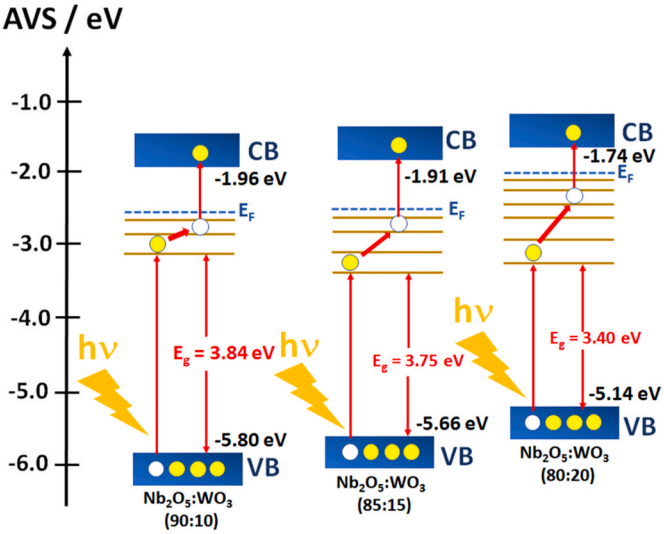

Fig. 8. Illustration of the energy band diagram of Nb_2O_5:WO_3 thin films with ratios of 90:10, 85:15, and 80:20.

and electrochromic applications. It is well known that standard DFT calculations using the GGA-PBE functional often underestimate the electronic band gaps of materials due to inadequate treatment of the exchange-correlation energy. Consequently, our calculated band gaps for Nb_2O_5 (1.84 eV) and WO_3 (1.28 eV) are significantly lower than the experimental values (3.84–3.40 eV). While more advanced methods, such as hybrid functionals or GW calculations [68–70], could provide

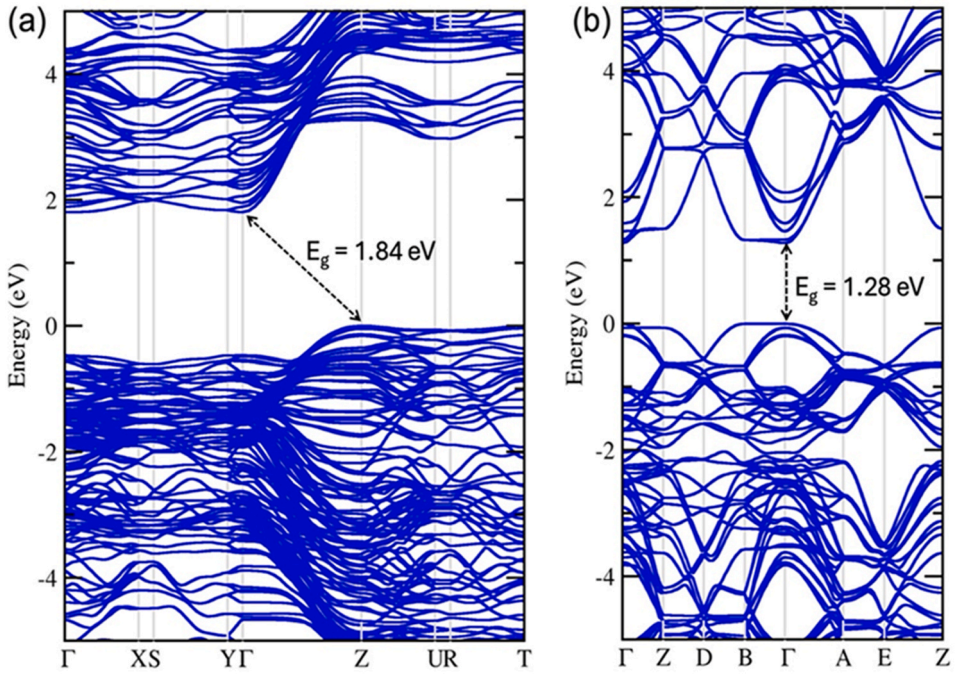

Fig. 9. Electronic band structures of (a) Nb_2O_5 and (b) WO_3 calculated using the GGA-PBE functional in DFT. The band gaps (E_g) of Nb_2O_5 and WO_3 are also shown.

improved accuracy, they are computationally expensive and beyond the scope of this study. Nonetheless, the trends observed in our calculations provide valuable insight into the electronic properties of these materials and their potential applications. The band structures illustrate the differences in the CB and VB dispersions, reflecting the impact of the local atomic environment and bonding on the electronic properties. Next, we investigated the effects of incorporating W into an Nb_2O_5 crystal. Because W has a smaller ionic radius than Nb, we considered only the case of W substituting for the Nb site. Two inequivalent Nb sites existed in the TT-Nb_2O_5 considered in the simulations. Our DFT calculations show that the substitutional W on the Nb site (W_{Nb}) shown in Fig. 10 is 0.22 eV lower in energy than another Nb site. Therefore, we consider this site to be energetically favorable for W_{Nb}.

The observed shrinkage of the W–O bond lengths when W substitutes for Nb in Nb_2O_5 can be attributed to the smaller ionic radius of W and its distinct bonding characteristics. The ionic radius of W^{5+} (~0.62–0.70 Å in octahedral coordination) is smaller than that of Nb^{5+} (~0.78 Å), contributing to the reduction in bond lengths. However, the contraction is further amplified by the stronger and more localized W–O bonds, driven by the higher electronegativity of W (2.36 for W compared with 1.6 for Nb on the Pauling scale). This increased electronegativity results in a greater Coulombic attraction between W^{5+} and the surrounding O^{2-} ions, pulling the oxygen atoms closer. The preference of W for forming stronger covalent bonds also induces local lattice relaxation, further shortening the W–O bonds relative to the equilibrium Nb–O bond lengths. These structural distortions reflect a balance between the smaller size of W and its chemical bonding tendencies, which together stabilize the substitutional sites.

In addition, our calculated band structure of the supercell with one W_{Nb}, in Fig. 11, corresponding to 6.3 % of W doping on the Nb lattice site, shows a bandgap reduction of approximately 0.16 eV. This

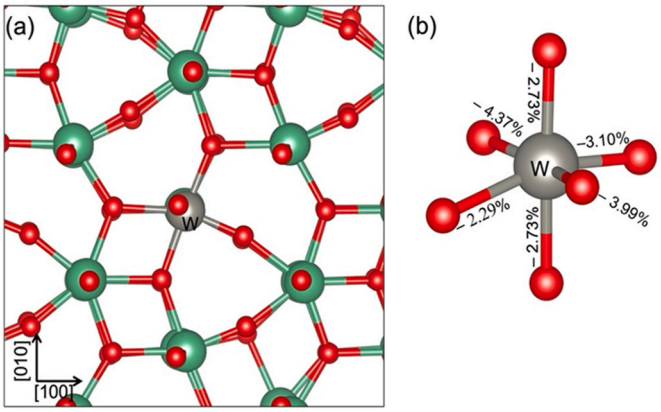

Fig. 10. (a) Relaxed local atomic structure of W substituted for Nb in Nb_2O_5 (W_{Nb}), showing the surrounding oxygen coordination in the Nb_2O_5 lattice. (b) Detailed atomic structure view of the W_{Nb} site illustrates the percentage change in W–O bond lengths relative to the equilibrium Nb–O bond lengths.

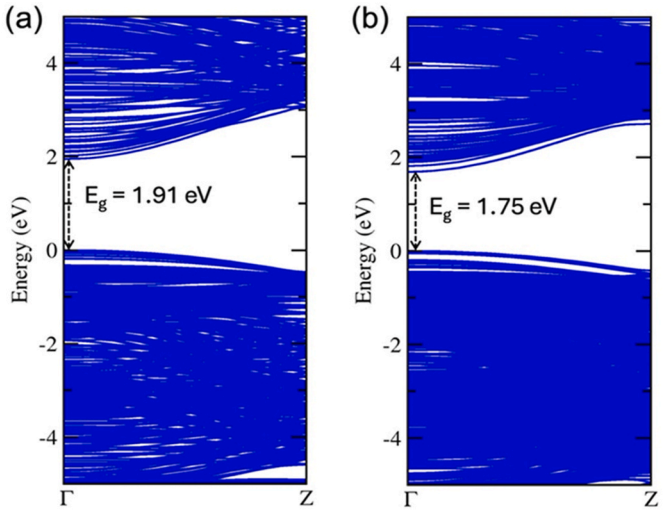

Fig. 11. Calculated band structure of (a) defect-free supercell and (b) the supercell with W_{Nb}. The band gaps of the supercells before and after W doping are also shown. Note that the band gap of the defect-free supercell slightly deviates from that of the primitive cell likely because of band folding in the supercell and computational parameters.

indicates that doping W into Nb_2O_5 results in a redshift in the light absorption, which is consistent with the experimental observations. Our results are consistent with previous reports on reduced absorption edges in chemically doped metal oxides such as TiO_2 [68] and $SrTiO_3$ [69].

The extinction coefficient or absorption index (k) was calculated from the absorption coefficient (α) and the wavelength of the incident light (λ) using Eq. (3) [71]:

$$k = \frac{\alpha\lambda}{4\pi}. \tag{3}$$

Fig. 12(a) shows the trend of k spectra, which increased with longer wavelength and increased with increasing WO_3 concentration. Average k values in the range of 350–1100 nm are 0.40×10^{-2}, 1.02×10^{-2}, and 3.89×10^{-2} for the Nb_2O_5:WO_3 (90:10), Nb_2O_5:WO_3 (85:15), and Nb_2O_5:WO_3 (80:20) thin films, respectively. The k values are very low and almost zero, indicating minimal optical losses owing to absorption and demonstrating the great optical quality of the thin films [72]. However, the increase in k values with increasing WO_3 content is due to the increase in the free carrier concentration [73] and greater extinction of atoms and electrons in the thin films, whereas more electrons can be excited from the VB to the CB [74,75]. In addition, the enhancement of the k value may be related to the increase in surface roughness, leading to enhanced scattering losses and corresponding to a decrease in optical transmittance [3]. The sudden increase in all thin film conditions in the UV region (300–350 nm) is ascribed to the absorption of photons by the thin films.

The absorption coefficient and photon energy are related to the properties of the thin films, and the absorption coefficient shows an exponential increase with photon energy near the high-energy side (energy gap). Such behavior is known as the Urbach edge in accordance with the following relation [36]:

$$\alpha(h\nu) = \alpha_0 \, exp\left(\frac{h\nu}{E_U}\right), \tag{4}$$

where α_0 is a constant and E_U is the Urbach energy, which is interpreted as the width of the CB tails at localized states associated with the structural disorder of the thin film, which can be determined from the slope of the plot of $\ln(\alpha)$vs. $h\nu$ in Fig. 12(b) as the relation $E_U = 1/slope$. Table 4 shows the E_U values from 172.58 to 182.28 meV for the Nb_2O_5:WO_3 (90:10) to Nb_2O_5:WO_3 (80:20) thin films. This increasing E_U value is due to increased localized defect states, as shown in the schematic in Fig. 8, demonstrating a strong correlation between the variation in the dislocation density. J. Vivekanandan et al. [3] also suggested that the amorphization trend of thin films with increasing WO_3 content contributes to the increase in Urbach energy, which is further supported by the XRD results in Fig. 2. This correlation is consistent with the findings reported for other thin film materials such as cobalt (Co) and aluminum (Al) co-doping in ZnO nanostructure [75], Cu-precoated MnS with different annealing temperatures [76], and fluorine-doped Sb_2O_3 [77].

3.4. Comparison of refractive indexes with different methods and packing densities

The static refractive index (n_0) of Nb_2O_5:WO_3 with different ratios is correlated to the energy band gap based on the Dimitrov–Sakka expression [78]:

$$n_0 = \left[6\sqrt{\frac{5}{E_g}} - 2\right]^{1/2}, \tag{5}$$

and the optical dielectric constant calculates from the refractive index $(\varepsilon_0 = n_0^2)$ [78].

As shown in Table 4, the n_0 values increased as the WO_3 concentration increased and varied from 2.201 to 2.297, while the ε_0 values varied from 4.847 to 5.276 for the highest WO_3 ratio. This suggests hyperpolarization and d-orbital transition of Nb and W in the thin film, consistent with the transition of Ni–O for the glass material [78,79]. Furthermore, a comparison of the refractive indices with different calculation models was performed and elaborated to further examine the optical properties of the Nb_2O_5:WO_3 thin films:

The Moss relation was used using the empirical relation as follows [80]:

$$n = \left(\frac{95\ eV}{E_g}\right)^{1/4}. \tag{6}$$

Similarly, Reddy and Ahammed altered Moss relationship as follows [81]:

$$n = \left(\frac{154\ eV}{E_g - 0.365}\right)^{1/4}. \tag{7}$$

Ravindra et al. proposed an alternative linear empirical relation of n with E_g as follows [82]:

$$n = K_1 - K_2 E_g, \tag{8}$$

where K_1 and K_2, determined through empirical fitting, are 4.084 and 0.62 $(eV)^{-1}$, respectively. Meanwhile, Herve and Vandamme presented the corresponding n vs. E_g relationship based on the classical oscillatory theory as follows [83]:

$$n = \sqrt{1 + \frac{A^2}{(E_g + B)^2}}, \tag{9}$$

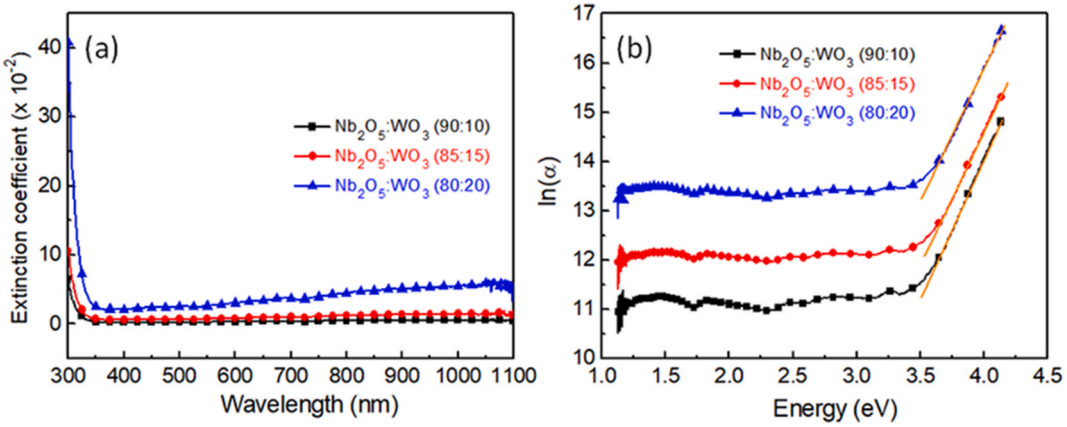

Fig. 12. (a) Extinction coefficient spectra and (b) plot of ln(α) vs. energy for Urbach energy determination of the Nb_2O_5:WO_3 thin films with ratios of 90:10, 85:15, and 80:20.

Table 4
Optical, dielectric constant parameters, and refractive index calculation proposed by different relationship models for Nb_2O_5:WO_3 thin films.

Nb_2O_5: WO_3 ratio	E_g (eV)	E_U (meV)	n_0	ε_0	n (Moss)	n (Reddy and Ahammed)	n (Ravindra)	n (Herve and Vandamme)	n (Kumar and Singh)	n (Ahmad and Haq)	n (Tripathy)	n (Gomaa)
90:10	3.84	172.58	2.201	4.847	2.230	2.580	1.703	2.112	2.182	2.254	2.145	2.046
85:15	3.75	182.26	2.220	4.928	2.243	2.597	1.759	2.133	2.199	2.272	2.166	2.063
80:20	3.40	182.28	2.297	5.276	2.299	2.669	1.976	2.218	2.269	2.348	2.256	2.136

where A and B are constants. A was found to be 13.6 eV by fitting, which corresponds to the hydrogen ionization energy, whereas B corresponds to the constant difference between the UV resonance energy and the energy gap, which is 3.47 eV. The Kumar and Singh equation for the calculation of n from E_g was obtained through the simulation process, as follows [84]:

$$n = KE_g^C, \tag{10}$$

where K and C have values of 3.3668 and −0.32234, respectively. The Ahmad and Haq model is presented as follows [85]:

$$n = \left(\frac{44}{E_g}\right)^{1/3}. \tag{11}$$

Furthermore, Tripathy expressed n vs. E_g dependence for various binary and ternary semiconductors with the relationship [86]:

$$n = n_0\left(1 + \alpha \exp\left(-\beta E_g\right)\right), \tag{12}$$

where $n_0 = 1.73$, $\alpha = 1.9017$, and $\beta = 0.539\ (\text{eV})^{-1}$. Finally, Gomaa et al. suggested the prediction of the refractive index from the band gap using the relationship [87]:

$$n = \left[\left(A \Big/ E_g^{\frac{1}{2}}\right) - B\right]^{1/2}, \tag{13}$$

when $A = 3.44^2$ and $B = 3.44^{1/2}$. In Table 4, the calculated n values according to the different relationship models are observed to increase with increasing WO_3 concentration and decreasing energy band gap. In more detail, Fig. 13(a) shows the trend of the refractive index vs. WO_3 concentration using different relationship models. From these calculation models, it can be noted that there is an inverse correlation between the refractive index and energy band gap, that is, a decreased E_g leads to an increased n, suggesting a slight increase in densification or packing density. Thus, the effect of the packing density (p) of the thin films was investigated and can be assessed to confirm the increase in refractive index with WO_3 concentration using the following relationship [88]:

$$n^2 = \frac{\left[(1-p)n_v^4 + (1+p)n_v n_s^2\right]}{(1+p)n_v^2 + (1-p)n_s^2}, \tag{14}$$

where n_v represents the refractive index of the voids ($n_v = 1$ for air), and n_s represents the refractive index of the borosilicate glass substrate (n_s =

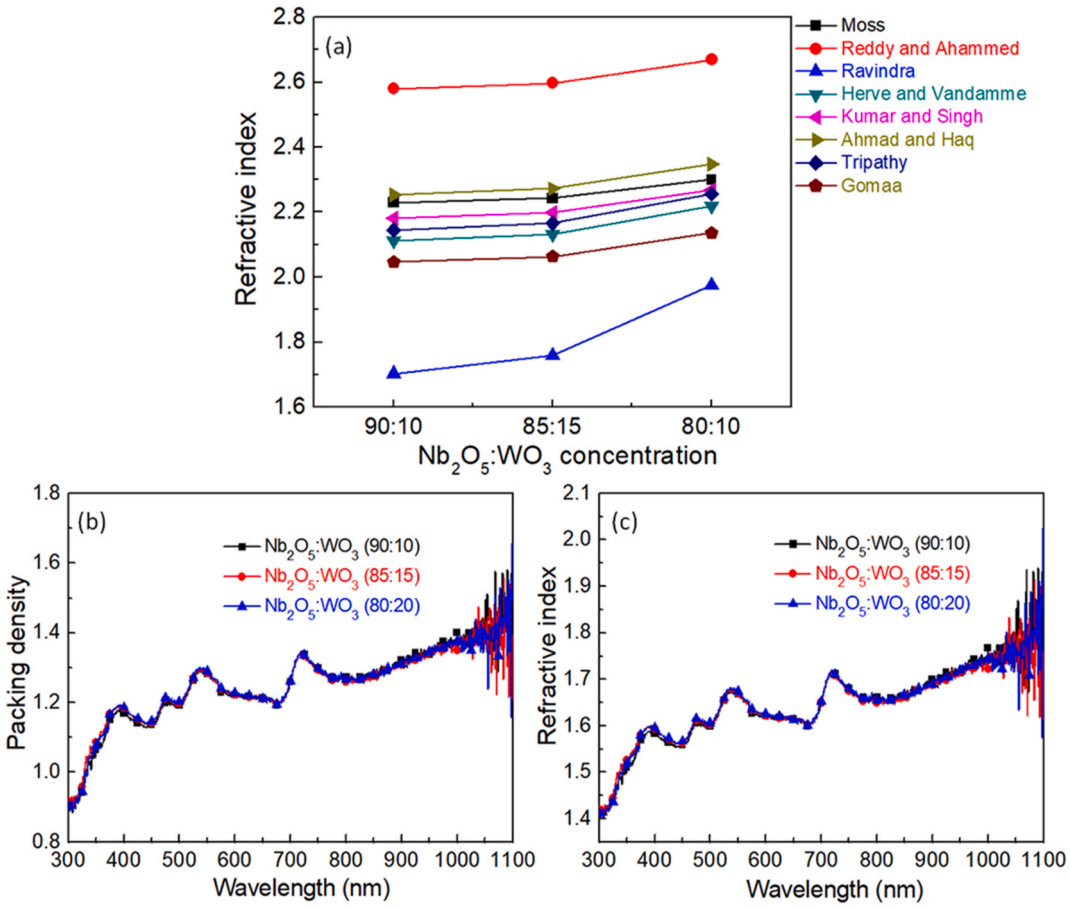

Fig. 13. (a) Plot of refractive index variation calculated using different empirical models of Nb_2O_5 with WO_3 concentration, (b) packing density, and (c) variation of refractive index spectra as a function of wavelength.

1.47) [89]. Fig. 13(b) displays the packing density vs. WO_3 concentration of the thin films. The average packing density values, in the wavelength range of 300–1000 nm, increased to 1.228, 1.230, and 1.232 as the WO_3 concentration increased, which is ascribed to the increase in the refractive index and surface roughness of the thin films.

The refractive index for each ratio of Nb_2O_5:WO_3 thin films in the UV, visible, and NIR regions was calculated using the relation with reflectance, as follows [90]:

$$n = \frac{1+\sqrt{R}}{1-\sqrt{R}}. \quad (15)$$

Similarly, the refractive index for each ratio of Nb_2O_5:WO_3 thin films, in Fig. 13(c), shows the same results as the packing density. The spectra are increased in the UV, visible, and NIR regions, which is also related to the packing density of the thin films [72]. The average refractive index values, in the range of 300–1000 nm, are increased to 1.629, 1.630, and 1.632 with increasing WO_3 concentration and increasing packing density. To confirm the consistency of the results, our refractive index values are close to the sample of a Nb_2O_5:TiO_2 nanocomposite thin film coated on an FTO glass substrate deposited by a thermionic vacuum arc (n = 1.73) [91]. It can be noted that increasing WO_3 concentration resulted in an amorphous-crystalline phase transition with a free-cracked nature and there is no porosity or inter-atomic spacing, resulting in the increasing densification of the films and refractive index [92]. H. Hu et al. also reported that increasing packing density would lead to a higher refractive index and decrease the band gap for the HfO_2 films [93].

The real (ε_1) and imaginary (ε_2) parts of the dielectric constants can be calculated using the following equations [77]:

$$\varepsilon_1 = n^2 - k^2. \quad (16)$$

$$\varepsilon_2 = 2nk. \quad (17)$$

HYPERLINK \l "Fig. 14" \o "Fig. 14" Fig. 14(a) shows that the real parts of dielectric constants and the spectra of Nb_2O_5:WO_3 thin films in each ratio are almost identical and increase as a function of wavelength, which indicates the higher optical response of the thin film in the UV, visible, and NIR regions and the average ε_1 values in the wavelength range of 300–1000 nm are 2.658, 2.662, and 2.664 with increasing WO_3 concentration. Meanwhile, the imaginary part of the dielectric constant, shown in Fig. 14(b), exhibits a sudden increase in the UV region, which demonstrates that the thin films have a very high optical response in the UV region owing to the high absorption of photons [3]. The average ε_2 values in the wavelength range of 350–1100 nm are 1.355, 3.428, and 13.072 with increasing WO_3 concentration. The increase in the average ε_1 and ε_2 values with increasing WO_3 concentration indicates that the synthesized thin films have greater electrical energy induced by the addition of WO_3 in the Nb_2O_5 structure, thereby enhancing the optical response of the synthesized thin films in accordance with a decrease in the dissipation rate of the incident light [3].

To assess the nature of chemical bonding with the ability of the doping atom to occupy the interstitial positions in the host lattice and atomic transformation from covalent to ionic in nature in the semiconductor thin films, we used the optical electronegativity (η_{opt}) calculated using the following equation [94]:

$$\eta_{opt} = \left[\frac{A}{n}\right]^{1/4}, \quad (18)$$

where n is the refractive index and A is a dimensionless constant with a value of 25.54 for all materials. Fig. 15(a) shows the changes in the η_{opt} spectra and the increase in decreasing wavelength of the incident light, which are inversely related to the refractive index in Fig. 13(c). The increasing average η_{opt} values of 1.7094, 1.7099, and 1.7103 are obtained with increasing WO_3 concentration. This result confirms that

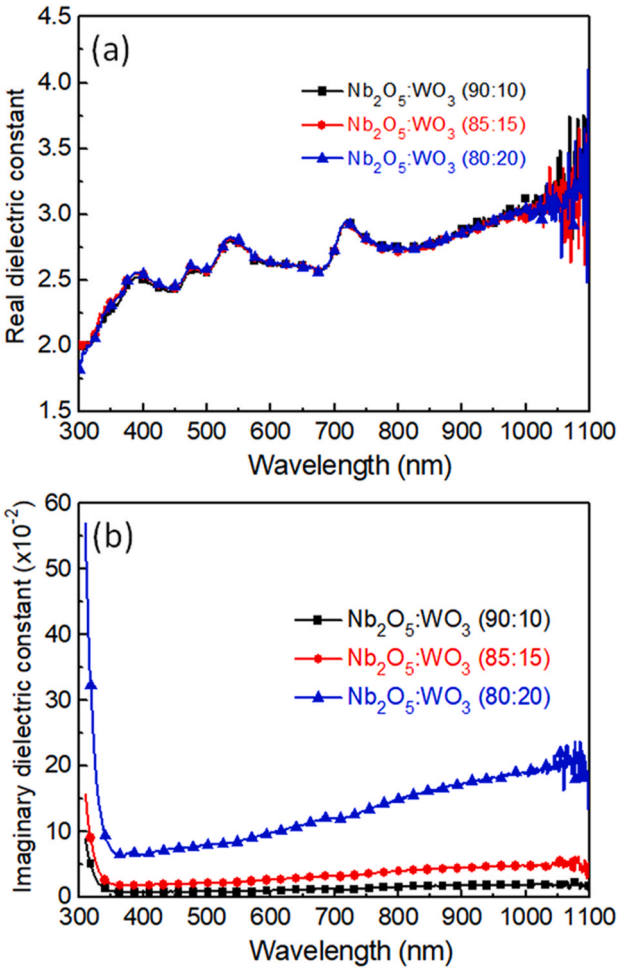

Fig. 14. Variation of (a) real and (b) imaginary parts of dielectric constant as a function of wavelength of the Nb_2O_5:WO_3 thin films with ratios of 90:10, 85:15, and 80:20.

more W atoms substitute in the interstitial sites of the Nb_2O_5 lattice, which is consistent with a previous report on Mg-doped ZnO thin films [95].

Based on the calculation of the optical electronegativity (η_{opt}), the electronic polarizability (α_e) of carriers in thin films and the optical basicity (Λ) are given by Eqs. (19) and (20), respectively [96],

$$\alpha_e = -0.9*\eta_{opt} + 3.5. \quad (19)$$

$$\Lambda = -1.5*\eta_{opt} + 1.7. \quad (20)$$

The plots of α_e are portrayed in Fig. 15(b) and the enhancement of α_e with increasing wavelength for the Nb_2O_5:WO_3 thin film at each ratio indicates electron volumes increase owing to more absorbed photons of the incident light in the UV, visible, and NIR regions. Furthermore, the average α_e values show an increasing trend of 1.7085, 1.7090, and 1.7093 as the WO_3 concentration increases because of the larger volume of electrons, that is, larger atoms have lightly bound electrons, whereas smaller atoms have tightly bound electrons in thin films [3]. Similarly, increasing optical basicity, as shown in Fig. 15(c), is obtained, with values of 0.7047, 0.7050, and 0.7052, as the WO_3 concentration increases because of the lower energy band gap, which indicates the lower energy used for electron donation in the bonded elements. Therefore, electrons are free to transfer between the VB to the CB in the thin film semiconductor [97].

We investigate the effect of the WO_3 concentration on the electrical conductivity. When the electrons absorb photon energy from the

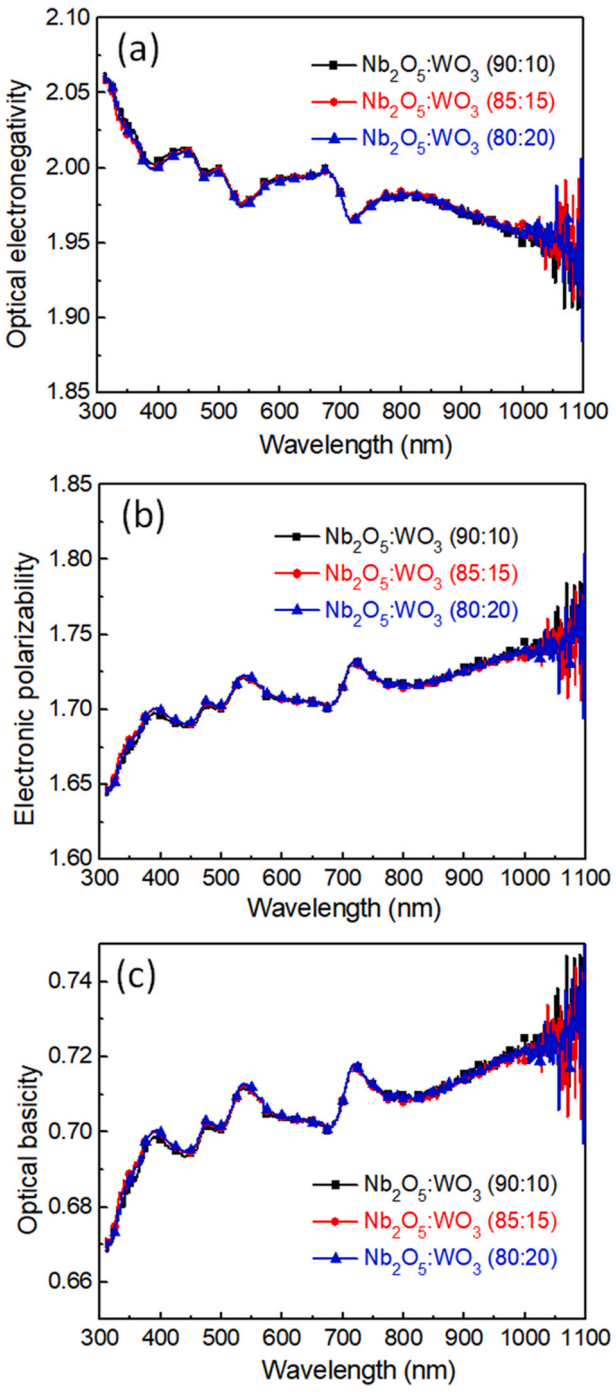

Fig. 15. (a) Optical electronegativity, (b) electronic polarizability, and (c) optical basicity of Nb_2O_5:WO_3 thin films with ratios of 90:10, 85:15, and 80:20.

incident light, the electrons will be excited to the CB and the thin film semiconductor becomes conductive. Thus, this mechanism can be observed by the photonic effect or the optical conductivity (σ_{opt}) and electrical conductivity (σ_{elec}), which are estimated from Eqs. (21) and (22), respectively [98]:

$$\sigma_{opt} = \frac{\alpha n c}{4\pi}. \tag{21}$$

$$\sigma_{elec} = \left(\frac{n}{k}\right)\sigma_{opt}. \tag{22}$$

As shown in Fig. 16(a), the optical conductivity enhances with the WO_3 concentration throughout the UV, visible, and NIR regions, which is attributed to the increase in the absorption of light photons. This is because the electrical conductivity of the Nb_2O_5:WO_3 thin films is strongly influenced by the band gap, as shown in Fig. 16(b). The increase in WO_3 concentration attributes to the contraction in the energy band gap, leading to an increase in electrical conductivity along the energy range from 1.0 to 4.5 eV region.

The volume (VELF) and surface (SELF) energy loss functions can be plotted using Eqs. (23) and (24), respectively [3]:

$$VELF = \frac{\varepsilon_2}{(\varepsilon_1^2 + \varepsilon_2^2)}. \tag{23}$$

$$SELF = \frac{\varepsilon_2}{(\varepsilon_1 + 1)^2 + \varepsilon_2^2}. \tag{24}$$

Fig. 17(a and b) shows the VELF and SELF spectra of the synthesized thin films with WO_3 concentration. VELF and SELF showed the same trend of increasing energy loss with increasing WO_3 concentration. The increase in energy loss originating from diffusion via the film surface or three-dimensional structure is due to the increase in photon absorption from the incident light [3,99].

3.5. Dispersion energy parameters

For a more comprehensive understanding of the optical properties of the thin films, the dispersion energy parameters oscillator energy (E_o) and dispersion energy (E_d) were calculated using the Wemple and DiDomenico model [59,77,94]:

$$n^2(h\nu) = 1 + \frac{E_o E_d}{E_o^2 - (h\nu)^2}. \tag{25}$$

The E_o and E_d values for the Nb_2O_5:WO_3 thin films were extracted from the slopes $(E_o E_d)^{-1}$ and intercepts (E_o/E_d) according to the derivation of the plot between $(n^2-1)^{-1}$ against $(h\nu)^2$ in Fig. 18(a). As shown in Table 5, the E_d and E_o values increased for the ratio of Nb_2O_5:WO_3 (90:10) and Nb_2O_5:WO_3 (85:15), and then decreased for the ratio of Nb_2O_5:WO_3 (80:20). Moreover, a WO_3 concentration higher than the optimum condition will decrease the atomic coordination number, which consequently decreases the change in the structural order of the thin films and the oscillator population of the Nb–O and W–O oscillators [100]. The correlation between E_o and E_g can also be functionally expressed by the average ratio of $E_o/E_g \approx 1.5$ [3], and the ratios obtained increased from 1.076 to 1.254. Meanwhile, the values of the oscillation strength (f) were reduced by exceeding the optimum WO_3 concentration owing to the decrease in the strength of the bonds, as shown in Table 5.

From the dispersion energy parameters, the first-order (M_{-1}) and third-order (M_{-3}) moments of the optical spectra were evaluated using the following relation [87]:

$$E_o^2 = \frac{M_{-1}}{M_{-3}}. \tag{26}$$

$$E_d^2 = \frac{M_{-1}^3}{M_{-3}}. \tag{27}$$

As shown in Table 4, M_{-1} is reduced to 2.1286 and 2.0807 $(eV)^2$ for Nb_2O_5:WO_3 (90:10) and Nb_2O_5:WO_3 (85:15), respectively, and increased slightly to 2.1084 $(eV)^2$ for Nb_2O_5:WO_3 (80:20). Meanwhile, M_{-3} is 0.1246 and 0.1082 $(eV)^{-2}$ for Nb_2O_5:WO_3 (90:10) and Nb_2O_5:WO_3 (85:15), respectively, and increased to 0.1160 $(eV)^{-2}$ for Nb_2O_5:WO_3 (80:20).

3.6. Optoelectrical parameters

The ratio of the optical free carrier concentration to effective mass (N_{opt}/m^*) and high-frequency lattice dielectric constant (ε_L) of the

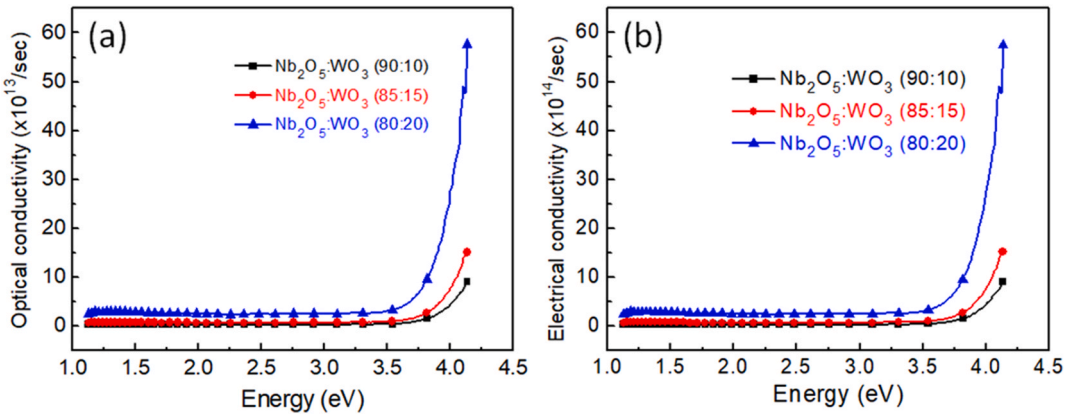

Fig. 16. (a) Optical conductivity and (b) electrical conductivity of Nb_2O_5:WO_3 thin films with ratios of 90:10, 85:15, and 80:20.

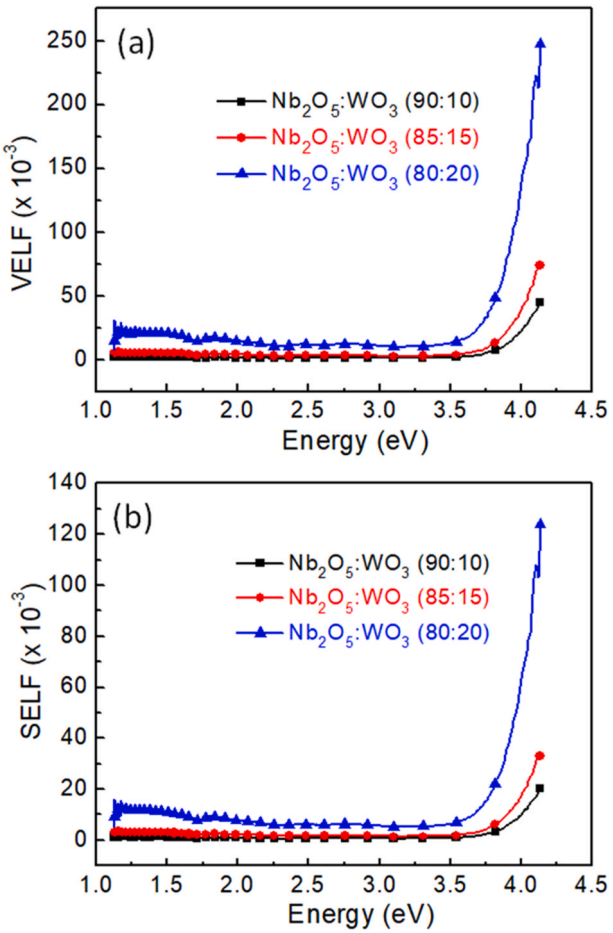

Fig. 17. Variation of (a) VELF and (b) SELF as a function of energy of Nb_2O_5:WO_3 thin films with ratios of 90:10, 85:15, and 80:20.

Nb_2O_5:WO_3 thin films were calculated using the following equation [18,61,88,100]:

$$\varepsilon_1 = n^2 = \varepsilon_L - \left(\frac{e^2}{4\pi^2 c^2 \varepsilon_0}\right)\left(\frac{N_{opt}}{m^*}\right)\lambda^2, \tag{28}$$

where e is the electronic charge, c is the velocity of light, and ε_0 is the free-space dielectric constant (8.854×10^{-12} F/m or $C^2/N{\cdot}m^2$). The plots of n^2 vs. λ^2 of the thin films at different ratios are displayed in Fig. 18(b), and the plasma resonance frequency (ω_p) can be determined from the slope of the plot of ε_1 and $1/\omega^2$ in Fig. 18(c). The intercept of the plot indicates the high-frequency dielectric constant (ε_∞) [61]:

$$\varepsilon_1 = \varepsilon_\infty - \frac{\omega_p^2}{\omega^2}, \tag{29}$$

where ω denotes the angular frequency. Moreover, the dielectric optical relaxation time is a property of solids that is related to the conductivity of the thin film, which is a measurement of how long the thin film takes to become neutralized by the conduction process. This parameter can be determined using the following relation [88]:

$$\omega_p \times \tau = 1. \tag{30}$$

Furthermore, the optical mobility (μ_{opt}) and optical resistivity (ρ_{opt}) of the Nb_2O_5:WO_3 thin films were calculated using the following equations [101]:

$$\mu_{opt} = \frac{e}{\omega_p \times m^*} = \frac{e\tau}{m^*}. \tag{31}$$

$$\rho_{opt} = \frac{1}{e \times \mu_{opt} \times N_{opt}}. \tag{32}$$

The effective mass of the electron–hole pair or exciton (m^*) for Nb_2O_5 is $0.532m_0 = 4.846 \times 10^{-31}$ kg, where m_0 is the rest mass of the electron, which is 9.11×10^{-31} kg [102]. The calculated optoelectrical parameters are summarized in Table 6. The variations in the optoelectrical parameters with the WO_3 concentration in Nb_2O_5 may indicate the presence of some interactions that occur between these photons from the incident light and free electrons of the thin films. Thus, the optimum WO_3 concentration may induce a slight increase in the rate of energy dispersion and decrease in the propagation velocity of the electromagnetic waves that fall on the thin films [101].

3.7. FT-IR analysis

Fig. 19 displays the FT-IR spectra of Nb_2O_5:WO_3 in different ratios. The results do not show remarkable differences due to the same structure, corroborated by the presence of a weak and broad peak around 755–756 cm^{-1}, which is assigned to the Nb–O–Nb bond [103]. However, this peak may also be assigned to the stretching vibration of the OH molecule and W–O–W groups [104]. In addition, a strong broad band peak around 891–899 cm^{-1} appears, corresponding to the O═Nb═O bond [103]. Finally, the weak and broad peak around 1073–1087 cm^{-1} is attributed to the absorption of CO_2 from the air or stretching vibrations of the C–O bond [105].

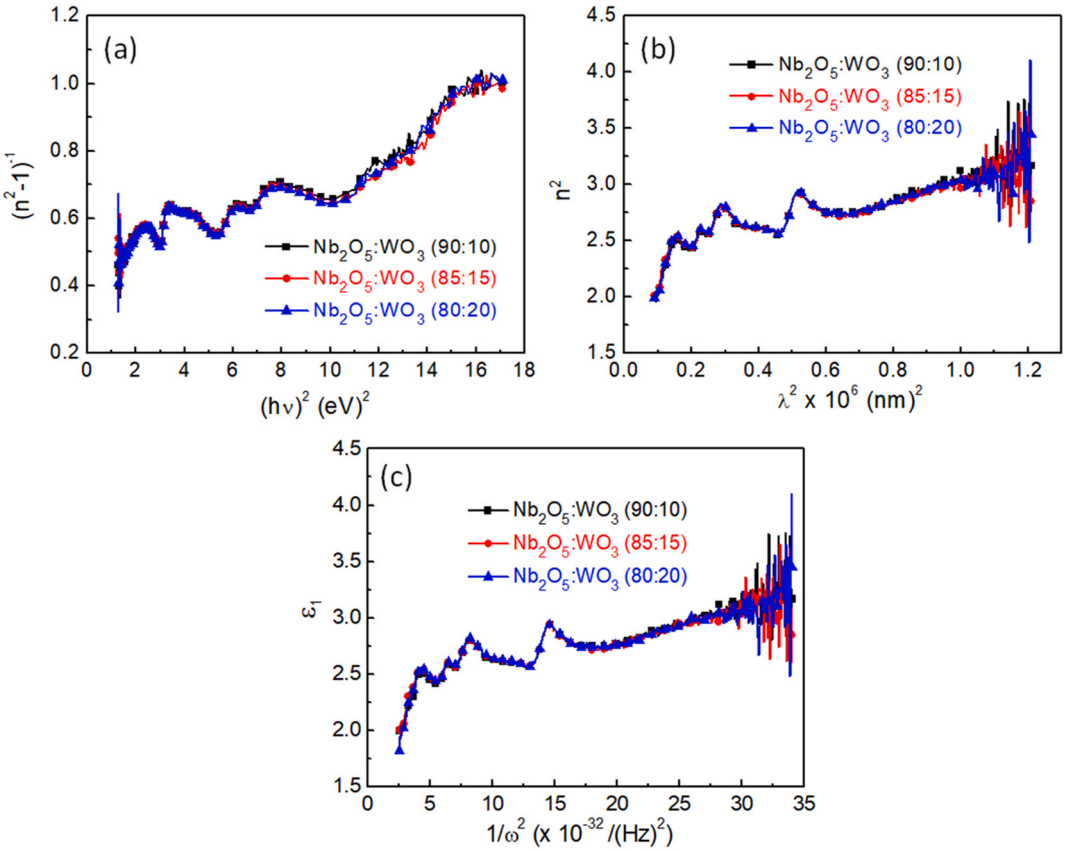

Fig. 18. Variation of $(n^2\text{-}1)^{-1}$ against $(h\nu)^2$ of Nb_2O_5:WO_3 thin films with ratios of 90:10, 85:15, and 80:20.

Table 5
Dispersion energy parameters of Nb_2O_5:WO_3 thin films.

Nb_2O_5:WO_3 ratio	Slope $(E_oE_d)^{-1}$	Intercept (E_o/E_d)	E_d (eV)	E_o (eV)	E_o/E_g	f (eV)^2	M_{-1} (eV)^2	M_{-3} (eV)$^{-2}$
90:10	0.0275	0.4698	8.7979	4.1332	1.076	36.364	2.1286	0.1246
85:15	0.0250	0.4806	9.1230	4.3845	1.169	40.000	2.0807	0.1082
80:20	0.0261	0.4743	8.9878	4.2629	1.254	38.314	2.1084	0.1160

Table 6
Optoelectrical parameters of Nb_2O_5:WO_3 thin films.

Nb_2O_5:WO_3 ratio	ε_L	N_{opt}/m^* (× 10^{56} kg^{-1} m^{-3})	N_{opt} (× 10^{26} m^{-3})	ε_∞	ω_p (× 10^{15} Hz)	τ (× 10^{-16} s)	μ_{opt} (× 10^{-4} C·sec/kg)	ρ_{opt} (× 10^{-5} kg m^3/C^2·sec)
90:10	2.306	9.429	4.570	2.305	1.652	6.053	1.998	6.844
85:15	2.350	8.303	4.024	2.345	1.550	6.452	2.130	7.292
80:20	2.344	8.596	4.166	2.339	1.580	6.329	2.090	7.180

3.8. Micro-Raman investigation

Micro-Raman spectroscopy was performed on Nb_2O_5:WO_3 (90:10), (85:15), and (80:20), and the results are shown in Fig. 20. The Raman spectra confirmed the existence of Nb_2O_5 and WO_3 in the thin films. The peak intensities centered at 560 and around 802–822 cm^{-1} are increased with increasing WO_3 concentration. The peak band in the 500–700 cm^{-1} centered at 560 cm^{-1} and the peak around 802–822 cm^{-1} are assigned to the symmetric stretching vibration mode of the bridging W–O–W bonds [106]. Meanwhile, the peak bands at 224 and 252 cm^{-1} are assigned to the bending modes of the Nb–O–Nb linkages. The major Raman band at ~306 cm^{-1} is assigned to the long and weak Nb–OH_2 bond. The band at ~629 cm^{-1} corresponds to a slightly different Nb–O bond distance and is assigned to the symmetric stretching mode of the NbO_6 octahedra, whereas the peak at ~685 cm^{-1} is related to the poorly distorted NbO_6 octahedral and pentagonal bipyramid structure coordination. Furthermore, the weak Raman band at ~990–993 cm^{-1} is associated with the symmetric and antisymmetric stretching modes of the Nb═O terminal bond [107]. These observed Raman bands confirm the presence of Nb_2O_5 in the Nb_2O_5:WO_3 (90:10) thin film. However, peaks at 224, 252, 306, 629, and 685 cm^{-1} are absent, which might be due to the higher WO_3 ratio incorporated in the Nb_2O_5 thin films. In general, the Raman spectrum of tungstate reflects tungsten sublattices, and the niobium element displays weak Raman activity as well as the nickel element [3]. Thus, the Raman band at 560 cm^{-1} for WO_3 becomes more dominant with increasing WO_3 concentration, whereas the peaks for Nb_2O_5 become weaker for Nb_2O_5:WO_3 (85:15) and (80:20). Consequently, more defects in the Nb_2O_5 crystal lattice indicate the incorporation of WO_3, which coincides with the optical absorption and Urbach energy performances [3].

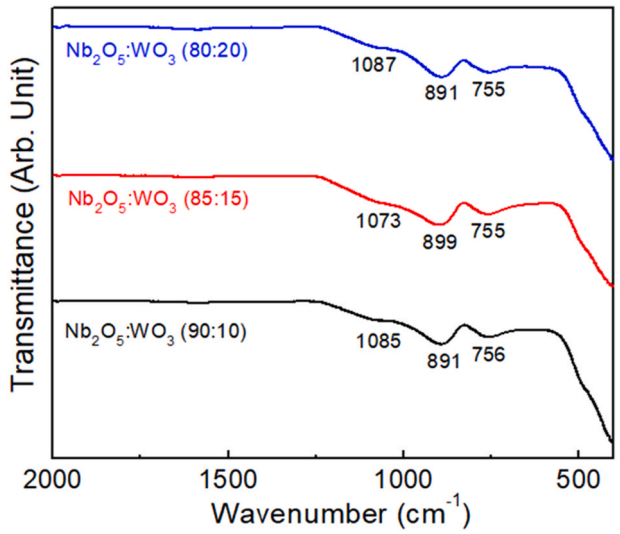

Fig. 19. FT-IR spectra of Nb_2O_5:WO_3 thin films with ratios of 90:10, 85:15, and 80:20.

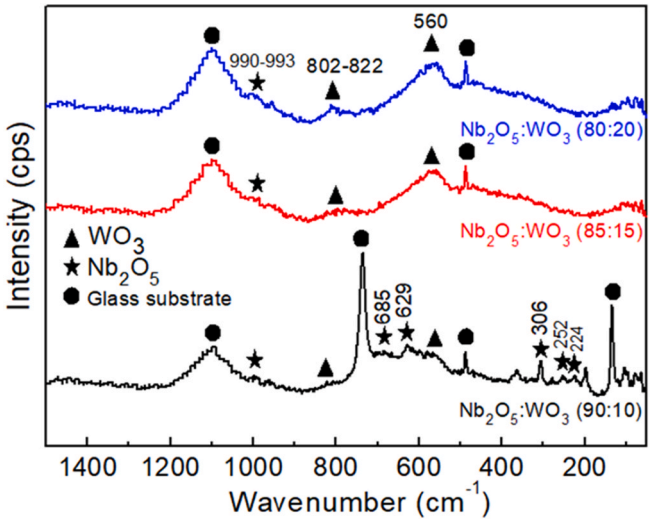

Fig. 20. Micro-Raman spectra of Nb_2O_5:WO_3 thin films with ratios of 90:10, 85:15, and 80:20.

3.9. Room temperature photoluminescence investigation

We investigated the electronic structure and electron transfer mechanism in the forbidden band gap of the semiconductor in terms of the location of defect levels, material imperfections, and impurities with respect to the top level of the VB and bottom level of the CB, which controls their luminescence properties [108]. Photoluminescence (PL) spectroscopy was performed to identify these issues. Fig. 21 displays the PL spectra of the Nb_2O_5:WO_3 thin films with ratios of 90:10, 85:15, and 80:20. The results show that a UV emission peak at ~254.46–254.58 nm is clearly observed for the Nb_2O_5:WO_3 thin film excited by a photoexcitation source at 255 nm. Then, an electron from the VB of Nb_2O_5 with an empty 4*d*-orbital of Nb^{5+} instead of the Nb^{4+} ions will be excited to a CM of Nb_2O_5 and enters a state that is bonded to the hole of W^{6+} as W^{6+} is a TM cation with an empty 3*d*-orbital. The FWHM of the peak is around 0.11–0.12 eV, with an excitation band at ~254.46–254.58 nm. The energy of the excitation band is approximately 4.87 eV, which is caused by the transfer of W^{6+} according to the following mechanism: VB $+ h\nu \longrightarrow W^{6+}$, and the main W^{6+} ions in the valence state of W change to W^{5+}. The ground-state configuration of W^{5+} is characterized by a single

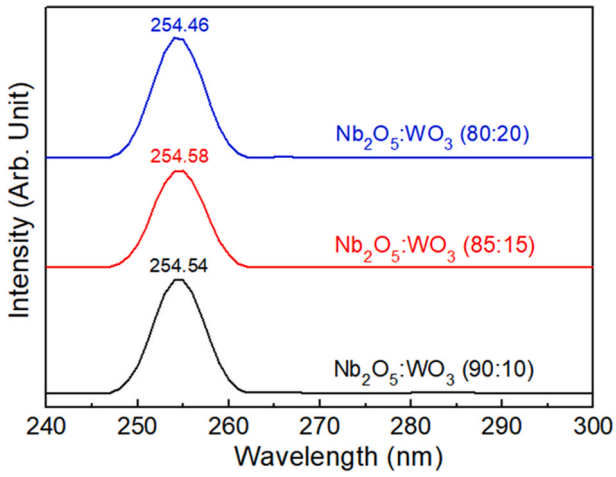

Fig. 21. Photoluminescence spectra of Nb_2O_5:WO_3 thin films with ratios of 90:10, 85:15, and 80:20.

5*d* electron outside a closed shell; that is, the ground term of W^{5+} also comprises a ground level and a metastable level with the creation of a hole on the neighboring oxygen [108,109]. J. Vivekanandan et al. also explained this mechanism; however, in our research, when WO_3 is incorporated into the Nb_2O_5 lattice, this may generate a defect-induced recombination process by a singly occupied oxygen vacancy, which leads to a reduction in the NBE peak. As the WO_3 concentration increases from 10 % to 15 %, the emission intensity may also decrease owing to nonradiative recombination. Higher intensity of the peak is observed when the WO_3 concentration increased to 20 %, which could be attributed to excess oxygen atoms, and the slight shift of the peak in each ratio condition could be consequently related to the change in the energy band gap of the thin films [3]. Notably, these shifts in the PL bands and energy band gap alterations can have future industrial applications in optoelectrical devices.

3.10. Linear and nonlinear optical susceptibility

The first-order optical linear susceptibility $(\chi^{(1)})$ and the third-order optical nonlinear susceptibility $(\chi^{(3)})$ are important parameters for investigating the optical properties of promising materials including third harmonic generation (THG), four-wave mixing (FWM), two-photon absorption (TPA), self-phase modulation (SPM), stimulated Raman scattering, as well as cross-phase modulation (XPM) [110] for ultrafast optical switching, optical circuits, photonic devices, upconversion laser amplification, and high-capacity communication electronics. We used Miller's relationships as follows [3,61,99,100]:

$$\chi^{(1)} = \frac{n^2 - 1}{4\pi} = \frac{E_o E_d}{4\pi\left[E_o^2 - (h\nu)^2\right]}, \tag{33}$$

$$\chi^{(3)} = A\left[\chi^{(1)}\right]^4 = A\left[\frac{E_o E_d}{4\pi\left[E_o^2 - (h\nu)^2\right]}\right]^4, \tag{34}$$

where A is a constant factor equal to 1.7×10^{-10} esu. Fig. 22(a and b) displays the deviation of $\chi^{(1)}$ and $\chi^{(3)}$ of the Nb_2O_5:WO_3 thin films with ratios of (90:10), (85:15), and (80:20) as a function of photon energy $(h\nu)$.

The trend of $\chi^{(1)}$ and $\chi^{(3)}$ spectra increase with a reduction in photon energy, which

could generally be correlated to the enlargement of the refractive indices with photon energy (reduction with the lower wavelength of the incident light [Fig. 13(c)]). Average $\chi^{(1)}$ values of 0.1316, 0.1320, and 0.1324 are obtained and slightly increased with WO_3 concentration,

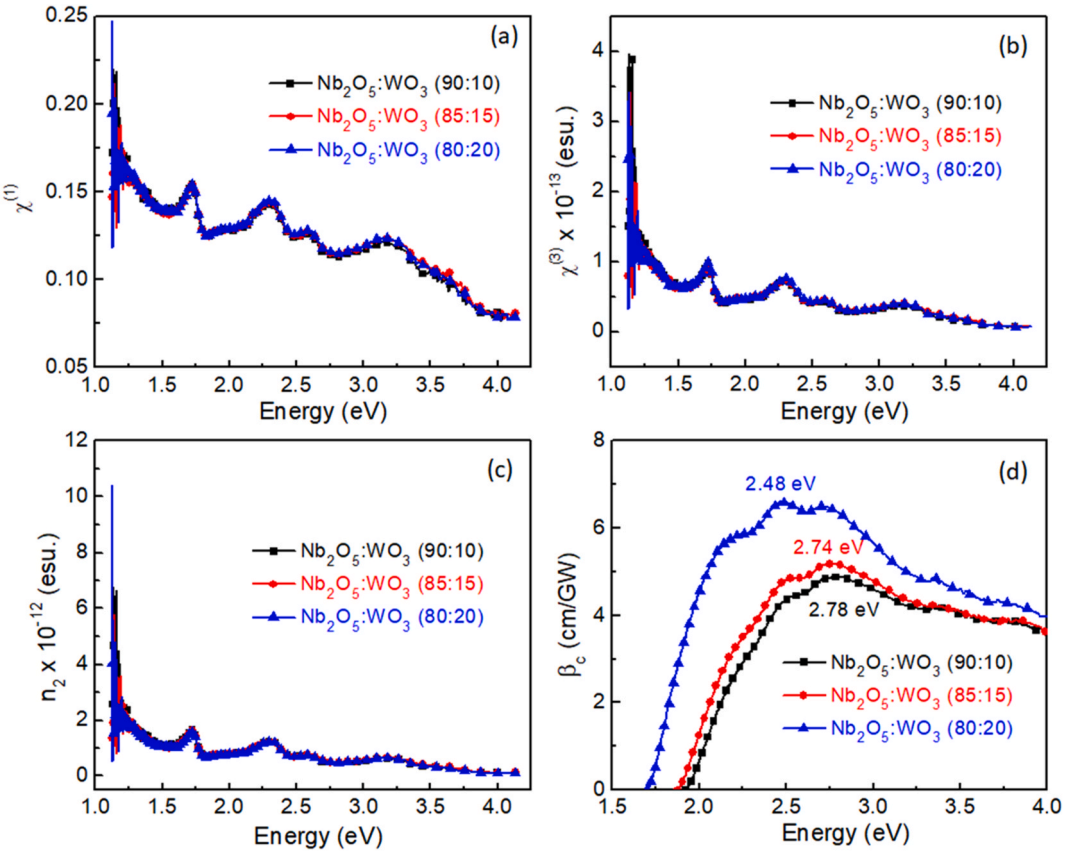

Fig. 22. Alteration of (a) the first-order, (b) third-order susceptibilities, (c) nonlinear refractive index, and (d) two-photon absorption coefficient as a function of energy of Nb_2O_5:WO_3 thin films with ratios of 90:10, 85:15, and 80:20.

whereas the average $\chi^{(3)}$ values are calculated to be 5.650 × 10^{-14}, 5.636 × 10^{-14}, and 5.734 × 10^{-14} esu. A slight decrease is observed in average $\chi^{(3)}$ values for the Nb_2O_5:WO_3 (85:15) thin films due to the decrease in E_d/E_o ratio. However, the overall increase in $\chi^{(1)}$ and $\chi^{(3)}$ values with increasing WO_3 concentration renders expansion in the 3D network of the thin films [61] and an increase in the strength of chemical bonding between the molecules of Nb_2O_5:WO_3, which is the same as the previous literatures for NiO:WO_3 thin films [3,88]. Therefore, the nonlinear trend corresponds to bound electrons that influence the electric field from the incident light in the thin film [61]. These results summarize that the variation in the $\chi^{(1)}$ and $\chi^{(3)}$ parameters are beneficial for UV nonlinear optical materials, window layers, solid-state lasers, and nonlinear optical device applications [61,111].

3.11. Nonlinear refractive index and two-photon absorption coefficient

Nonlinear refractive index (n_2) is also the useful parameter for evaluating the material in a

Wide range of optical limiting applications, including optical frequency conversion, optical signal processing, and laser devices, which can be obtained using the following relationship [47,112]:

$$n_2 = \frac{12\pi\chi^{(3)}}{n_0}, \tag{35}$$

where n_0 denotes the static refractive index. The spectra of n_2 are shown in Fig. 22(c) and exhibit the same trend as $\chi^{(3)}$ for the NiO:WO_3 thin films. The average n_2 values were determined to be 1.20 × 10^{-12}, 1.14 × 10^{-12}, and 1.13 × 10^{-12} esu. with an increase in the WO_3 concentration. Then, the empirical relation developed by Sheik-Bahae et al. for the two-photon absorption coefficient (β_c) indicates that these two photons are absorbed at the same time to excite an atom, molecule, or ion to a higher energy state. Based on the linear optical parameters, i.e., linear refractive index (n) and energy band gap (E_g), the spectra of β_c are displayed in Fig. 22(d), according to the following equation [47,112]:

$$\beta_c = \frac{K\sqrt{E_p}}{n^2 E_g^3}\frac{\left[(2h\nu/E_g)-1\right]^{3/2}}{(2h\nu/E_g)^5}, \tag{36}$$

where K is the scaling factor (3100 cm/GW), E_p indicates the Kane momentum energy and is nearly material independent for a wide range of various semiconductors (~21 eV). The applicable photon energy range is $\frac{E_g}{2} < h\nu < E_g$, which satisfies the two-photon absorption coefficient conditions. It can be seen that the variation of β_c with the energy of the incident photon and the values of β_c increased as energy increased until reaching a maximum point, after which the spectra subsequently decreased and the maximum value of β_c exists ~0.7 times of the E_g value. The energy values at a maximum point of β_c are decreased from 2.78 to 2.48 eV with increasing WO_3 concentration, which may be ascribed to a reduction in the E_g value. The same behavior was also observed in other studies, such as octaethylporphyrin (PtOEP) thin film [47], Ag/$Ge_{20}Se_{50}S_{30}$ bilayer film [112], and lead bromide ($CH_3NH_3PbBr_3$) perovskite film [113].

Among optoelectronic devices, the Nb_2O_5 and WO_3 material can be synthesized as a stacking Nb_2O_5 passivation of WO_3 thin film to prevent electrochromic performance degradation in heated water and moist conditions [114]. WO_3-doped Nb_2O_5 thin films have been deposited via reactive co-sputtering of niobium and tungsten metal targets at room temperature for electrochromic devices, sensors, and solar cells [115]. In addition, composite WO_3–Nb_2O_5 thin films were successfully prepared using a simple and inexpensive spray pyrolysis technique as a working electrode to investigate their electrochemical performances and

further employed as promising electrochemical devices [116]. Finally, Nb-doped hexagonal WO_3 nanowire-modified graphite was used as a positive electrode in vanadium redox flow batteries [117].

4. Conclusions

The effects of WO_3 concentration on Nb_2O_5 in terms of structural, morphological, compositional, dispersion energy, and linear/nonlinear optical properties were investigated. The findings of our novel research can be summarized as follows.

(I) Some crystal grains or residuals increased, and the thickness of the film was reduced from 2.40 μm to 0.40 μm with increasing WO_3 concentration.
(II) The increasing WO_3 concentration in the Nb_2O_5 lattice modified the structure from crystalline to amorphous, which is advantageous for the ion diffusion pathway in thin films.
(III) The lower thickness led to more residuals, high-density natural defects, and surface roughness, which were attributed to a greater light scattering effect, demonstrating lower crystalline quality in the synthesized thin films. A lower transmittance value from ~74 to 67 % as the increasing absorption coefficient value from 0.73 $\times 10^3$ to 7.00 $\times 10^3$ cm^{-1} with increasing WO_3 concentration was obtained owing to the higher photon absorption ability in the thin film since the reflectance of the thin film is less than 10 %.
(IV) Increasing WO_3 concentration led to the decrease in E_g values from 3.84 ± 0.01 to 3.40 ± 0.02 eV owing to the occurrence of localized states created between the CB and VB. The correlation of n and E_g using different empirical models showed that the n values increased with WO_3 concentration owing to increased packing density.
(V) The standard DFT calculations using the GGA-PBE functional yielded calculated band gaps for Nb_2O_5 of 1.84 eV and WO_3 of 1.28 eV, which are significantly lower than the experimental values (3.84 ± 0.01 − 3.40 ± 0.02 eV). However, the trends observed in our calculations provide valuable insight into the electronic properties of these materials and their potential applications.
(VI) The WO_3 concentration induces variations in the optoelectrical parameters due to the presence of some interactions between photons from the incident light and free electrons of the thin films. Thus, the optimum WO_3 concentration may induce a slight increase in the rate of energy dispersion and a decrease in the propagation velocity of the electromagnetic waves that fall on the thin films.
(VII) FT-IR and micro-Raman results revealed the bonding of the precursors in the synthesized thin films. Meanwhile, in the PL spectra, an electron from the VB of Nb_2O_5 with an empty 4*d*-orbital of Nb^{5+} instead of the Nb^{4+} ions is excited to a CM of Nb_2O_5 and enters into a state that is bonded to the hole of W^{6+} as W^{6+} is a TM cation with an empty 3*d*-orbital.
(VIII) The overall increase in average $\chi^{(1)}$ and $\chi^{(3)}$ but decrease in average n_2 values of 0.1316–0.1324, 5.636 $\times 10^{-14}$ to 5.734 $\times 10^{-14}$ esu., and 1.20 $\times 10^{-12}$ to 1.13 $\times 10^{-12}$ esu., respectively, as the energy values at a maximum point of β_c are decreased from 2.78 to 2.48 eV with increasing WO_3 concentration rendered the expansion in the 3D network of the thin films and increase in strength of chemical bonding between the molecules of Nb_2O_5: WO_3, which may be ascribed to a reduction in the E_g value.
(IX) The results of this study demonstrates that the synthesized thin films are beneficial for UV nonlinear optical material, window layer, solid-state laser and can produce affordable promising nonlinear optical device applications.

CRediT authorship contribution statement

Panupat Chaiworn: Writing – original draft, Visualization, Validation, Investigation, Funding acquisition, Formal analysis, Data curation. **Watcharin Teerananattapong:** Writing – original draft, Visualization, Validation, Investigation, Formal analysis, Data curation. **Pakpoom Reunchan:** Writing – original draft, Visualization, Validation, Investigation, Formal analysis, Data curation. **Auttasit Tubtimtae:** Writing – original draft, Validation, Supervision, Resources, Methodology, Formal analysis, Conceptualization. **Ekasiddh Wongrat:** Writing – review & editing, Writing – original draft, Visualization, Validation, Investigation, Funding acquisition, Formal analysis, Data curation.

Ethical approval

The research article is in compliance with Ethical Standards.

Author agreement

The authors declare that this study has not been published previously and is not currently submitted elsewhere. All authors have read the paper and agree with its submission to **Optical Materials**. We have read and understood your journal's policies and there are no conflicts of interest to declare.

Declaration of competing interest

The authors declare that they have no known competing financial interests or personal relationships that could have appeared to influence the work reported in this paper.

Acknowledgment

We would like to acknowledge the financial support from Chiang Mai Rajabhat University, Thailand. Also, this research was supported by University of Phayao and Thailand Science Research and Innovation Fund (Fundamental Fund 2024).

Data availability

The authors confirm that data supporting the findings of this study are available within the article.

References

[1] N.A. Ibrahim, Nanomaterials for Antibacterial Textiles, Elsevier Inc., 2015, https://doi.org/10.1016/B978-0-12-801317-5.00012-8.
[2] Z. Tariq, S.U. Rehman, X. Zhang, F.K. Butt, S. Feng, B.U. Haq, B. Cheng, C. Li, Vanadium based zinc spinel oxides: potential materials as photoanode for water oxidation and optoelectronic devices, Int. J. Hydrogen Energy 46 (2021) 28110–28120, https://doi.org/10.1016/j.ijhydene.2021.06.073.
[3] J. Vivekanandan, K.S. Usha, R. Sivakumar, C. Sanjeeviraja, Influence of tungsten oxide concentration on structural, morphological, compositional, linear and nonlinear optical properties, and vibrational properties on NiO:WO_3 thin films, Opt. Mater. 144 (2023) 114313, https://doi.org/10.1016/j.optmat.2023.114313.
[4] S. Laurent, S. Boutry, R.N. Muller, Metal Oxide Particles and Their Prospects for Applications, Elsevier Ltd., 2018, https://doi.org/10.1016/b978-0-08-101925-2.00001-2.
[5] M. Hasanah, S. Susilawati, A. Ramadhan, Performance optimization of CuO-ZnO ceramic electrode on the electrocoagulation of wastewater, Mater. Sci. Energy Technol. 6 (2023) 7–14, https://doi.org/10.1016/j.mset.2022.11.001.
[6] F. Gillissen, M. Lobet, J. Dewalque, P. Colson, G. Spronck, R. Gouttebaron, M. Duttine, B. Faceira, A. Rougier, L. Henrard, R. Cloots, A. Maho, Mixed molybdenum-tungsten oxide as dual-band, VIS-NIR selective electrochromic material, ACS Symp. Ser. Am. Chem. Soc. https://doi.org/10.26434/chemrxiv-2024-vhf83..
[7] Y. Abe, Y. Kadowaki, M. Kawamura, K.H. Kim, T. Kiba, Two-color electrochromic devices using a tungsten oxide and nickel oxide double layer, Jpn. J. Appl. Phys. 62 (2023) 015502, https://doi.org/10.35848/1347-4065/aca4b1.
[8] D.R. Rosaline, A. Suganthi, G. Vinodhkumar, S.S.R. Inbanathan, Ahmad Umar, Sadia Ameen, M.S. Akhtar, E.L. Foletto, Enhanced sunlight-driven photocatalytic activity of SnO_2-Sb_2O_3 composite towards emerging contaminant degradation in

water, J. Alloys Compd. 897 (2022) 162935, https://doi.org/10.1016/j.jallcom.2021.162935.
[9] M.A. Ashrafi, M. Ranjbar, H. Kalhori, H. Salamati, Pulsed laser deposition of Mo-V-O thin films for chromogenic applications, Thin Solid Films 621 (2017) 220–228, https://doi.org/10.1016/j.tsf.2016.11.041.
[10] S. Kim, J.H. In, S.H. Kim, K. Han, D. Lim, Y.S. Hwang, K.M. Lee, J.H. Choi, Study of high transmittance of SiO_2/Nb_2O_5 multilayer thin films deposited by plasma-assisted reactive magnetron sputtering, Appl. Sci. 13 (2023) 13271, https://doi.org/10.3390/app132413271.
[11] Z.S. Yuan, J.M. Jhang, P.H. Yu, C.M. Jiang, Y.C. Huang, Y.L. Wu, J.J. Lin, C. F. Yang, Comparisons of theoretical and experimental results of blue light SiO_2-Nb_2O_5 distributed bragg reflector fabricated using e-beam deposition, Vacuum 182 (2020) 109782, https://doi.org/10.1016/j.vacuum.2020.109782.
[12] J. Han, Y. Lan, Z. Xu, Y. Xu, H. Zhang, Nb_2O_5 film optical properties and laser-induced damage by phase-change-driven tuning, Ceram. Int. 50 (2024) 32330–32337, https://doi.org/10.1016/j.ceramint.2024.06.040.
[13] H.C. Fals, L.A. Lourençato, M.S. Orozco, M.J.X. Belém, C.R.C. Lima, Slurry erosion resistance of thermally sprayed Nb_2O_5 and Nb_2O_5+ $WC_{12}Co$ composite coatings deposited on AISI 1020 carbon steel, Ceram. Int. 46 (2020) 27670–27678, https://doi.org/10.1016/j.ceramint.2020.07.264.
[14] W. Ai, S. Xiong, Structural and optical properties of Nb_2O_5 films prepared by dual ion assisted deposition, Opt. Laser Technol 150 (2022) 107850, https://doi.org/10.1016/j.optlastec.2022.107850.
[15] C.L. Ücker, F.C. Riemke, N.F. de Andrade Neto, A.de A.G. Santiago, T. J. Siebeneichler, N.L.V. Carreño, M.L. Moreira, C.W. Raubach, S. Cava, Influence of Nb_2O_5 crystal structure on photocatalytic efficiency, Chem. Phys. Lett. 764 (2021) 138271, https://doi.org/10.1016/j.cplett.2020.138271.
[16] H. Xu, H. Li, Regulating the crystal phase of Pd/Nb_2O_5 for vanillin selective HDO at room temperature, J. Catal. 423 (2023) 105–117, https://doi.org/10.1016/j.jcat.2023.04.010.
[17] G.H.M. Gomes, S.J. Olusegun, J.B. Gabriel, R.C.V. Costa, N.D.S. Mohallem, The role of crystalline Nb_2O_5 nanoparticles for enhanced dye adsorption and photodegradation, Ceram. Int. 49 (2023) 6164–6176, https://doi.org/10.1016/j.ceramint.2022.10.126.
[18] K.T.G. Carvalho, A.E. Nogueira, O.F. Lopes, G. Byzynski, C. Ribeiro, Synthesis of g-C_3N4/Nb_2O_5heterostructures and their application in the removal of organic pollutants under visible and ultraviolet irradiation, Ceram. Int. 43 (2017) 3521–3530, https://doi.org/10.1016/j.ceramint.2016.11.063.
[19] A.M. Al-Baradi, M.M. El-Nahass, A.M. Hassanien, A.A. Atta, M.S. Alqahtani, A. O. Aldawsari, Influence of RF sputtering power on structural and optical properties of Nb_2O_5 thin films, Optik 168 (2018) 853–863, https://doi.org/10.1016/j.ijleo.2018.05.020.
[20] O.A. Jassim, S.G. Khalil, M.M. Mutter, Synthesis of nanostructured Al-doped Nb_2O_5 thin films using DC sputtering plasma for the gas sensors applications, Mater. Sci. Forum 1050 (2022) 9–20, https://doi.org/10.4028/www.scientific.net/MSF.1050.9.
[21] M.A. de Araújo, M.F. Gromboni, F. Marken, S.C. Parker, L.M. Peter, J. Turner, H. C. Aspinall, K. Black, L.H. Mascaro, Contrasting transient photocurrent characteristics for thin films of vacuum-doped "grey" TiO_2 and "grey" Nb_2O_5, Appl. Catal. B Environ. 237 (2018) 339–352, https://doi.org/10.1016/j.apcatb.2018.05.065.
[22] S. Sathasivam, B.A.D. Williamson, S.A. Althabaiti, A.Y. Obaid, S.N. Basahel, M. Mokhtar, D.O. Scanlon, C.J. Carmalt, I.P. Parkin, Chemical vapor deposition synthesis and optical properties of Nb_2O_5 thin films with hybrid functional theoretical insight into band structure and band gaps, ACS Appl. Mater. Interfaces 9 (2017) 18031–18038, https://doi.org/10.1021/acsami.7b00907.
[23] H.F. Khazaal, I.S. Hburi, M.S. Farhan, The impact of ion-beam parameters on the characteristics of Nb_2O_5 thin films, Surfaces Interf. 20 (2020) 100593, https://doi.org/10.1016/j.surfin.2020.100593.
[24] G. Falk, M. Borlaf, M.J. Lopez-Munoz, J.B.R. Neto, R. Moreno, Microwave-assisted synthesis of Nb_2O_5 for photocatalytic application of nanopowders and thin films, J. Mater. Res. 32 (2017) 3271–3278, https://doi.org/10.1557/jmr.2017.93.
[25] M.A. Fakhri, F.G. Khalid, E.T. Salim, Influence of annealing temperatures on Nb_2O_5 nanostructures prepared using pulsed laser deposition method, J. Phys.: Conf. Ser. 1795 (2021) 012063, https://doi.org/10.1088/1742-6596/1795/1/012063.
[26] A. Amato, G. Cagnoli, M. Granata, B. Sassolas, J. Degallaix, D. Forest, C. Michel, L. Pinard, N. Demos, S. Gras, M. Evans, A. Di Michele, M. Canepa, Optical and mechanical properties of ion-beam-sputtered Nb_2O_5 and TiO_2-Nb_2O_5 thin films for gravitational-wave interferometers and an improved measurement of coating thermal noise in Advanced LIGO, Phys. Rev. D 103 (2021) 072001, https://doi.org/10.1103/PhysRevD.103.072001.
[27] X. Chen, R. Bai, M. Huang, Optical properties of amorphous Ta_2O_5 thin films deposited by RF magnetron sputtering, Opt. Mater. 97 (2019) 109404, https://doi.org/10.1016/j.optmat.2019.109404.
[28] P. Gao, H. Wang, P. Li, W. Gao, Y. Zhang, J. Chen, N. Jia, In-site synthesis molecular imprinting Nb_2O_5-based photoelectrochemical sensor for bisphenol A detection, Biosens. Bioelectron. 121 (2018) 104–110, https://doi.org/10.1016/j.bios.2018.08.070.
[29] N. Akkurt, S. Pat, R. Mohammadigharehbagh, A. Olkun, Ş. Korkmaz, Electrochromic properties of graphene doped Nb_2O_5 thin film, ECS J. Solid State Sci. Technol. 9 (2020) 125004, https://doi.org/10.1149/2162-8777/abd079.
[30] N. Usha, R. Sivakumar, C. Sanjeeviraja, M. Arivanandhan, Niobium pentoxide (Nb_2O_5) thin films: rf Power and substrate temperature induced changes in physical properties, Optik 126 (2015) 1945–1950, https://doi.org/10.1016/j.ijleo.2015.05.036.
[31] M.N. Polyanskiy, Refractiveindex.info database of optical constants, Sci. Data 11 (2024) 94, https://doi.org/10.1038/s41597-023-02898-2.
[32] H. Huang, C. Wang, J. Huang, X. Wang, Y. Du, P. Yang, Structure inherited synthesis of N-doped highly ordered mesoporous Nb_2O_5 as robust catalysts for improved visible light photoactivity, Nanoscale 6 (2014) 7274–7280, https://doi.org/10.1039/c4nr00505h.
[33] X. Wang, H. Zhang, J. Li, L. Jin, C. Liu, Y. Liao, K. Liu, Influence of Bi_2O_3-Nb_2O_5 additive on microstructure and magnetic properties of LiZn ferrites, J. Magn. Magn Mater. 564 (2022) 170165, https://doi.org/10.1016/j.jmmm.2022.170165.
[34] D. Manzani, T. Gualberto, J.M.P. Almeida, M. Montesso, C.R. Mendonça, V.A. G. Rivera, L.D. Boni, M. Nalin, S.J.L. Ribeiro, Highly nonlinear $Pb_2P_2O_7$-Nb_2O_5 glasses for optical fiber production, J. Non-Cryst. Solids 443 (2016) 82–90, https://doi.org/10.1016/j.jnoncrysol.2016.04.019.
[35] L. She, Q. Li, F. Zhang, L. Kang, X. He, J. Sun, Z. Lei, Z.H. Liu, Sulfur doping induced anionic oxidation of niobium-pentoxide-based anode for ultralong-life and high energy-density Na-ion capacitors, J. Power Sources 451 (2020) 227744, https://doi.org/10.1016/j.jpowsour.2020.227744.
[36] H. Chen, A. Chiasera, C. Armellini, G. Speranza, S. Varas, O. Sayginer, A. Alfano, M. Cassinelli, M. Caironi, R. Suriano, M. Zaghloul, A. Tagliaferri, M. Ferrari, S. M. Pietralunga, Near-IR transparent conductive amorphous tungsten oxide thin layers by non-reactive radio-frequency magnetron sputtering, EPJ Web Conf. 255 (2021) 05003, https://doi.org/10.1051/epjconf/202125505003.
[37] G.A. Niklasson, C.G. Granqvist, Electrochromics for smart windows: thin films of tungsten oxide and nickel oxide, and devices based on these, J. Mater. Chem. 17 (2007) 127–156, https://doi.org/10.1039/B612174H.
[38] K. Hong, K. Kim, S. Kim, I. Lee, H. Cho, S. Yoo, H.W. Choi, N.Y. Lee, Y.H. Tak, J. L. Lee, Optical properties of $WO_3/Ag/WO_3$ multilayer as transparent cathode in top-emitting organic light emitting diodes, J. Phys. Chem. C 115 (2011) 3453–3459, https://doi.org/10.1021/jp109943b.
[39] Y. Wang, B. He, H. Wang, J. Xu, T. Ta, W. Li, Q. Wang, S. Yang, Y. Tang, B. Zou, Transparent $WO_3/Ag/WO_3$ electrode for flexible organic solar cells, Mater. Lett. 188 (2017) 107–110, https://doi.org/10.1016/j.matlet.2016.11.054.
[40] D.B. Migas, V.L. Shaposhnikov, V.E. Borisenko, Tungsten oxides. I. Effects of oxygen vacancies and doping on electronic and optical properties of different phases of WO_3, J. Appl. Phys. 108 (2010) 093714, https://doi.org/10.1063/1.3505688.
[41] F. Menchini, L. Serenelli, L. Martini, A. Albano, P. Mangiapane, E. Salza, G. Stracci, G. de Cesare, D. Caputo, M. Tucci, Transparent WO_x window layers for silicon based heterojunction solar cells. IEEE 46th Photovoltaic Specialists Conference (PVSC), 2019, pp. 2699–2701, https://doi.org/10.1109/PVSC40753.2019.8980805. Chicago, IL, USA.
[42] T.P. Mabate, N.P. Maqunga, S. Ntshibongo, M. Maumela, N. Bingwa, Metal oxides and their roles in heterogeneous catalysis: special emphasis on synthesis protocols, intrinsic properties, and their influence in transfer hydrogenation reactions, SN Appl. Sci. 5 (2023) 196, https://doi.org/10.1007/s42452-023-05416-6.
[43] B.G. Ghule, R.S. Mane, Chapter 13 - chemical bath deposition for metal oxide nanostructures, solution methods for metal oxide nanostructures, Metal Oxides) (2023) 267–292, https://doi.org/10.1016/B978-0-12-824353-4.00004-X.
[44] A. Mazzi, N. Bazzanella, M. Orlandi, R. Edla, N. Patel, R. Fernandes, A. Miotello, Physical vapor deposition of mixed-metal oxides based on Fe, Co and Ni as water oxidation catalysts, Mater. Sci. Semicond. Process. 42 (2016) 155–158, https://doi.org/10.1016/j.mssp.2015.08.006.
[45] T. Murayama, K. Nakajima, J. Hirata, K. Omata, E.J.M. Hensene, W. Ueda, Hydrothermal synthesis of a layered-type W–Ti–O mixed metal oxide and its solid acid activity, Catal. Sci. Technol. 7 (2017) 243–250, https://doi.org/10.1039/C6CY02198K.
[46] E. Petrucci, M. Orsini, F. Porcelli, S.D. Santis, G. Sotgiu, Effect of spin coating parameters on the electrochemical properties of ruthenium oxide thin films, Electrochem 2 (2021) 83–94, https://doi.org/10.3390/electrochem2010008.
[47] A.A. Abuelwafa, T. Soga, S. Elnobi, Optimized structural, optical, and electrical properties of spin-coated Pt(II) octaethylporphyrin thin films for optoelectronic applications, Optik 295 (2023) 171538, https://doi.org/10.1016/j.ijleo.2023.171538.
[48] D.A. Ajadi, S.M. Agboola, O. Adedokun, Effect of spin coating speed on some optical properties of ZnO thin films, J. Chem. Eng. Mater. Sci. 4 (2016) 1–6, https://doi.org/10.4236/msce.2016.45001.
[49] M. Özgür, S. Pat, Ş. Korkmaz, Curie temperatures of manganese chalcogenide monolayers, Int. J. Hydrogen Energy 34 (2009) 5218–5222, https://doi.org/10.1016/j.ijhydene.2009.02.001.
[50] G. Kresse, J. Furthmüller, Efficiency of ab-initio total energy calculations for metals and semiconductors using a plane-wave basis set, Comput. Mater. Sci. 6 (1996) 15–50, https://doi.org/10.1016/0927-0256(96)00008-0.
[51] G. Kresse, J. Hafner, Ab initio molecular dynamics for liquid metals, Phys. Rev. B 47 (1993) 558–561, https://doi.org/10.1103/PhysRevB.47.558.
[52] J.P. Perdew, K. Burke, M. Ernzerhof, Generalized gradient approximation made simple, Phys. Rev. Lett. 77 (1996) 3865–3868, https://doi.org/10.1103/PhysRevLett.77.3865.
[53] G.H.M. Gomes, N.D.S. Mohallem, Insights into the TT-Nb_2O_5 crystal structure behavior, Mater. Lett. 318 (2022) 132136, https://doi.org/10.1016/j.matlet.2022.132136.
[54] K.S. Usha, R. Sivakumar, C. Sanjeeviraja, Vasant Sathe, V. Ganesan, T.Y. Wang, Improved electrochromic performance of a radio frequency magnetron sputtered

NiO thin film with high optical switching speed, RSC Adv. 6 (2016) 79668–79680, https://doi.org/10.1039/C5RA27099E.
[55] N. Akkurt, S. Pat, R. Mohammadigharehbagh, A. Olkun, Ş. Korkmaz, Electrochromic properties of graphene doped Nb_2O_5 thin film, ECS J. Solid State Sci. Technol. 9 (2020) 125004, https://doi.org/10.1149/2162-8777/abd079.
[56] Q. Wang, Z. Na, L. Yu, S. Dai, M.K. Nazeeruddin, H. Yang, Smart photovoltaic windows for next-generation energy-saving buildings, Adv. Sci. 11 (2024) 2407177.
[57] E. Pehlivan, F.Z. Tepehan, G.G. Tepehan, Comparison of optical, structural and electrochromic properties of undoped and WO_3-doped Nb_2O_5 thin films, Solid State Ion 165 (2003) 105–110, https://doi.org/10.1016/j.ssi.2003.08.021.
[58] A.L.D. Lima, H.V. Fajardo, A.E. Nogueira, M.C. Pereira, L.C.A. Oliveira, J. P. Mesquita, A.C. Silva, Selective oxidation of aniline into azoxybenzene catalyzed by Nb-peroxo@iron oxides at room temperature, N.J. Chem. 44 (2020) 8710–8717, https://doi.org/10.1039/d0nj00520g.
[59] I.M. El Radaf, A.R. Wassel, Structural and optical characterizations of the thermally evaporated $Pb_xGa_{1-x}Se$ thin films, Optik 238 (2021) 166610, https://doi.org/10.1016/j.ijleo.2021.166610.
[60] V. Şenay, S. Pat, Ş. Korkmaz, T. Aydoğmuş, S. Elmas, S. Özen, N. Ekem, M. Z. Balbağ, ZnO thin film synthesis by reactive radio frequency magnetron sputtering, Appl. Surf. Sci. 318 (2014) 2–5, https://doi.org/10.1016/j.apsusc.2013.10.044.
[61] M.S. El-Bana, M.S. Alkhalifah, I.M. El Radaf, Novel and promising material ($CuInSn_3S_8$) for photovoltaic and optoelectronic applications, Surface. Interf. 31 (2022) 102037, https://doi.org/10.1016/j.surfin.2022.102037.
[62] S. Elnobi, A.A. Abuelwafa, M.S. Abd El-sadek, H.S. Wasly, Facile synthesis and physical properties of magnesium dititanate nanoparticles for antibacterial applications, Indian J. Phys. 98 (2024) 2417–2427, https://doi.org/10.1007/s12648-023-03028-9.
[63] D. Sahoo, P. Priyadarshini, D. Alagarasan, R. Ganesan, S. Varadharajaperumal, R. Naik, Influence of top layer on the linear and nonlinear optical parameters of Ag(Te)/$As_{50}Se_{50}$ bilayer thin films, Indian J. Phys. 96 (2022) 267–274, https://doi.org/10.1007/s12648-020-01957-3.
[64] S.U. Awan, S.K. Hasanain, G.H. Jaffari, D.H. Anjum, U.S. Qurashi, Defects induced luminescence and tuning of bandgap energy narrowing in ZnO nanoparticles doped with Li ions, J. Appl. Phys. 116 (2014) 083510, https://doi.org/10.1063/1.4894153.
[65] W. Wang, A. Janotti, C.G. Van de Walle, Role of oxygen vacancies in crystalline WO_3, J. Mater. Chem. C 4 (2016) 6641–6648.
[66] J. Sancho-Parramon, V. Janicki, H. Zorc, Compositional dependence of absorption coefficient and band-gap for Nb_2O_5–SiO_2 mixture thin films, Thin Solid Films 516 (2008) 5478–5482.
[67] J. Nguu, F. Nyongesa, R. Musembi, B. Aduda, Electrophoretic deposition and characterization of TiO_2/Nb_2O_5 composite thin films for dye sensitized solar cells, J. Mater. Phys. Chem. 6 (2018) 1–8.
[68] S. Charoenphon, A. Boonchun, D. Jarukanont, J. T-Thienprasert, P. Reunchan, Energetics and optical properties of carbon impurities in rutile TiO_2, RSC Adv. 10 (2020) 19648–19654, https://doi.org/10.1039/D0RA02709J.
[69] P. Reunchan, N. Umezawa, A. Janotti, J. T-Thienprasert, S. Limpijumnong, Energetics and optical properties of nitrogen impurities in $SrTiO_3$ from hybrid density-functional calculations, Phys. Rev. B 95 (2017) 205204, https://doi.org/10.1103/PhysRevB.95.205204.
[70] Y. Kang, G. Kang, H.H. Nahm, S.H. Cho, Y.S. Park, S. Han, *GW* calculations on post-transition-metal oxides, Phys. Rev. B 89 (2014) 165130, https://doi.org/10.1103/PhysRevB.89.165130.
[71] I.S. Yahia, G.F. Salem, J. Iqbal, F. Yakuphanoglu, Linear and nonlinear optical discussions of nanostructured Zn-doped CdO thin films, Phys. B Condens. Matter 511 (2017) 54–60, https://doi.org/10.1016/j.physb.2017.01.030.
[72] C.V. Ramana, G. Baghmar, E.J. Rubio, M.J. Hernandez, Optical constants of amorphous, transparent titanium-doped tungsten oxide thin films, ACS Appl. Mater. Interfaces 5 (2013) 4659–4666, https://doi.org/10.1021/am4006258.
[73] M.F. Al-mudhaffer, Optical properties, interband transition strength and the surface, volume energy loss function of titanium dioxide film, J. Basrah Res. 36 (2010) 31–37.
[74] M.S. Dawood, T.A. Elmosalami, W.M. Desoky, Enhancement of elastic, optical and opto-electrical properties of Ni-Substituted $CoFe_2O_4$ nanoparticles with different concentrations, Opt. Mater. 117 (2021) 111101, https://doi.org/10.1016/j.optmat.2021.111101.
[75] S. Hajer, O. Khaldi, A. Dahri, N. Abdelmoula, I. Hammami, M.P.F. Graça, Z. Benzarti, Influence of (Co+Al) co-doping on structural, micro-structural, optical and electrical properties of nanostructured zinc oxide, Ceram. Int. 50 (2024) 44151–44164, https://doi.org/10.1016/j.ceramint.2024.08.264.
[76] H.M. Ali, E. Kh Shokr, A.A. Ismail, Moumen S. Kamel, H.A. Mohamed, M. F. Hasaneen, Doping and precoating by Cu-metal and annealing impacts on some physical properties and applications of MnS thin films, Opt. Mater. 148 (2024) 114821, https://doi.org/10.1016/j.optmat.2023.114821.
[77] A.S. Hassanien, I.M. El Radaf, Effect of fluorine doping on the structural, optical, and electrical properties of spray deposited Sb_2O_3 thin films, Mater. Sci. Semicond. Process. 160 (2023) 107405, https://doi.org/10.1016/j.mssp.2023.107405.
[78] W.S. AbuShanab, E.B. Moustafa, A.H. Hammad, R.M. Ramadan, A.R. Wassel, Enhancement the structural, optical and nonlinear optical properties of cadmium phosphate glasses by nickel ions, J. Mater. Sci. Mater. Electron. 30 (2019) 18058–18064, https://doi.org/10.1007/s10854-019-02158-3.
[79] Z. Zhenyu, S. Jiatian, S. Zhenrong, L. Jian, H. Wenhai, W. Zugeng, Nonlinear optical properties of Eu_2O_3 doped 5ZnO-20Nb_2O_5-75TeO_2 glasses, Chin. Sci. Bull. 49 (2004) 2446–2448, https://doi.org/10.1007/BF03183710.
[80] T.S. Moss, A relationship between the refractive index and the infra-red threshold of sensitivity for photoconductors, Proc. Phys. Soc. Sect. B 63 (1950) 167, https://doi.org/10.1088/0370-1301/63/3/302.
[81] R. Reddy, Y.N. Ahammed, A study on the Moss relation, Infrared Phys. Technol. 36 (1995) 825–830, https://doi.org/10.1016/1350-4495(95)00008-M.
[82] N. Ravindra, S. Auluck, V. Srivastava, On the Penn gap in semiconductors, Phys. Status Solidi (b) 93 (1979) K155–K160, https://doi.org/10.1002/pssb.2220930257.
[83] P. Hervé, L. Vandamme, General relation between refractive index and energy gap in semiconductors, Infrared Phys. Technol. 35 (1994) 609–615, https://doi.org/10.1016/1350-4495(94)90026-4.
[84] V. Kumar, J. Singh, Model for calculating the refractive index of different materials, Indian J, Pure Appl. Phy. 48 (2010) 571–574.
[85] S. Ahmad, M.M. Haq, A study of energy gap, refractive index and electronic polarizability of ternary chalcopyrite semiconductors, Iran, J. Phys. Res. 14 (2014) 89–93.
[86] S.K. Tripathy, Refractive indices of semiconductors from energy gaps, Opt. Mater. 46 (2015) 240–246, https://doi.org/10.1016/j.optmat.2015.04.026.
[87] H.M. Gomaa, I.S. Yahia, H.Y. Zahran, Correlation between the static refractive index and the optical bandgap: review and new empirical approach, Physica B Condens. Matter. 620 (2021) 413246–413247, https://doi.org/10.1016/J.physb.2021.413246.
[88] K.S. Usha, R. Sivakumar, C. Sanjeeviraja, M. Ichimura, Physical properties of rf magnetron sputter deposited NiO:WO_3 thin films, Mater. Res. Express 2 (2015) 016401, https://doi.org/10.1088/2053-1591/2/1/016401.
[89] H.G. Tompkins, S. Smith, D. Convey, Optimizing the ellipsometric analysis of a transparent layer on glass, Surf. Interface Anal. 29 (2000) 845–850, https://doi.org/10.1002/1096-9918(200012)29:12<845::AID-SIA938>3.0.CO, 2-Q.
[90] L.N. Okoli, I.A. Ezenwa, C.I. Elekalachi, O.T. Okpaneje, V.C. Okoye, Time optimization of chemically deposited cadmium silver sulphide (CdAgS) ternary thin films at room temperature, Phys. J. 2 (2016) 88–95.
[91] N.A. Özgür, S. Pat, R. Mohammadigharehbagh, Ş. Korkmaz, Substrate effect on electrochromic properties of Nb_2O_5:TiO_2 nanocomposite thin films deposited by thermionic vacuum arc, Vacuum 202 (2022) 111186, https://doi.org/10.1016/j.vacuum.2022.111186.
[92] R.K. Bhuyan, T.S. Kumar, A. Perumal, P. Saravanan, D. Pamu, Effect of annealing and atmosphere on the structure and optical properties of Mg_2TiO_4 thin films obtained by the radio frequency magnetron sputtering method, J. Exp. Nanosci. 8 (2012) 371–381, https://doi.org/10.1080/17458080.2012.690894.
[93] H. Hu, C.X. Zhu, Y.F. Lu, Y. Liew, M.F. Li, B.J. Cho, W.K. Chio, N. Yakovlev, Physical and electrical characterization of HfO_2 metal-insulator-metal capacitors for Si analog circuit application, J. Appl. Phys. 94 (2003) 551–557, https://doi.org/10.1063/1.1579550.
[94] I.M. El Radaf, Dispersion parameters, linear and nonlinear optical analysis of the $SnSb_2S_4$ thin films, Appl. Phys. A 126 (2020) 357, https://doi.org/10.1007/s00339-020-03543-0.
[95] A. El Hamidi, E. El Mahboub, K. Meziane, A. El Hichou, A. Almaggoussi, The effect of electronegativity on optical properties of Mg doped ZnO, Optik 241 (2021) 167070, https://doi.org/10.1016/j.ijleo.2021.167070.
[96] X. Zhao, X. Wang, H. Lin, Z. Wang, A new approach to estimate refractive index, electronic polarizability, and optical basicity of binary oxide glasses, Phys. B Condens. Matter 403 (2008) 2450–2460, https://doi.org/10.1016/j.physb.2008.01.009.
[97] K. Dagenais, M. Chamberlin, C. Constantin, Modeling energy band gap as a function of optical electronegativity for binary oxides, J. Young Investig. 25 (2013) 73–78.
[98] H.M. Gomaa, I.S. Yahia, Toward a novel and accurate relationship between electrical and optical conductivity in opto-material sciences: new strategy, J. Comput. Electron. 21 (2022) 1396–1403, https://doi.org/10.1007/s10825-022-01943-4.
[99] A.A. Abuelwafa, M.S. Abd El-sadek, S. Elnobi, T. Soga, Effect of transparent conducting substrates on the structure and optical properties of tin (II) oxide (SnO) thin films: comparative study, Ceram. Int. 47 (2021) 13510–13518, https://doi.org/10.1016/j.ceramint.2021.01.209.
[100] M.S. AlKhalifah, I.M. El Radaf, Structural, optoelectrical analysis, and optical properties of indium-doped Al_2O_3 thin films synthesized by spray pyrolysis, Optik 259 (2022) 168972, https://doi.org/10.1016/j.ijleo.2022.168972.
[101] A.S. Hassanien, Intensive linear and nonlinear optical studies of thermally evaporated amorphous thin Cu-Ge-Se-Te films, J. Non-Cryst. Solids 586 (2022) 121563, https://doi.org/10.1016/j.jnoncrysol.2022.121563.
[102] S. Dhawan, T. Dhawan, A.G. Vedeshwar, Growth of Nb_2O_5 quantum dots by physical vapor deposition, Mater. Lett. 126 (2014) 32–35, https://doi.org/10.1016/j.matlet.2014.03.107.
[103] A.A. Atta, A.M. Hassanien, M.M. El-Nahass, A.A. Shaltout, Y.A. Al-Talhi, A. M. Aljoudi, Influence of argon flow rate on structural and optical properties of transparent Nb_2O_5 thin films, Opt. Quantum Electron. 51 (2019) 341, https://doi.org/10.1007/s11082-019-2054-y.
[104] J. Jayachandiran, M. Arivanandhan, O. Padmaraj, R. Jayavel, D. Nedumaran, Investigation on ozone-sensing characteristics of surface sensitive hybrid rGO/WO_3 nanocomposite films at ambient temperature, Adv. Compos. Hybrid Mater. 3 (2020) 16–30, https://doi.org/10.1007/s42114-020-00134-8.
[105] R. Bhargava, S. Khan, Fabrication of WO_3–reduced graphene oxide (WO_3–G) nanocomposite for enhanced optical and electrical properties, J. Mater. Sci.

Mater. Electron. 31 (2020) 8370–8384, https://doi.org/10.1007/s10854-020-03372-0.
[106] E.I. Ross-Medgaarden, I.E. Wachs, Structural determination of bulk and surface tungsten oxides with UV-vis diffuse reflectance spectroscopy and Raman spectroscopy, J. Phys. Chem. C 111 (2007) 15089–15099, https://doi.org/10.1021/jp074219c.
[107] J.M. Jehng, I.E. Wachs, Structural chemistry and Raman spectra of niobium oxides, Chem. Mater. 3 (1991) 100–107, https://doi.org/10.1021/cm00013a025.
[108] P. Dorenbos, Charge transfer bands in optical materials and related defect level location, Opt. Mater. 69 (2017) 8–22, https://doi.org/10.1016/j.optmat.2017.03.061.
[109] A. Müller, S. Schippers, J. Hellhund, A.L.D. Kilcoyne, R.A. Phaneuf, B. M. McLaughlin, Photoionization of tungsten ions: experiment and theory for W^{5+}, J. Phys. B: At. Mol. Opt. Phys. 52 (2019) 195005 https://doi.org/10.1088/1361-6455/ab39c8.
[110] A.A. Abuelwafa, A. El-Denglawey, M. Dongol, M.M. El-Nahass, T. Soga, Influence of annealing temperature on structural and optical properties of nanocrystalline platinum octaethylporphyrin (PtOEP) thin films, Opt. Mater. 49 (2015) 271–278, https://doi.org/10.1016/j.optmat.2015.09.032.
[111] X. Dong, L. Huang, Q. Liu, H. Zeng, Z. Lin, D. Xu, G. Zou, Perfect balance harmony in $Ba_2NO_3(OH)_3$: a beryllium-free nitrate as a UV nonlinear optical material, Chem. Commun. 54 (2018) 5792–5795, https://doi.org/10.1039/C8CC03007C.
[112] M.S. Ebied, A.F. Elhady, M. Dongol, A.A. Abuelwafa, Thermal annealing induced modification in linear and nonlinear optical properties of $Ag/Ge_{20}Se_{50}S_{30}$ bilayer film, Opt. Mater. 148 (2024) 114962, https://doi.org/10.1016/j.optmat.2024.114962.
[113] E. Rueda, J. Serna, J.I. Uribe, D. Ramírez, F. Jaramillo, J. Osorio, H. García, Nonlinear two-photon absorption in the near-infrared band for lead bromide perovskite films using an F-scan nonlinear spectrometer, ACS Omega 7 (2022) 29100–29105, https://doi.org/10.1021/acsomega.2c02967.
[114] D. Lee, J.H. Hong, K.M. Kang, S. Oh, M. Shin, S.H. Han, Y.C. Nah, D.H. Kim, Nb_2O_5 passivation of WO_3 thin films to prevent electrochromic performance degradation in heated water, J. Alloys Compd. 967 (2023) 171569, https://doi.org/10.1016/j.jallcom.2023.171569.
[115] R. Sultana, K. Islam, S. Chakraborty, Tuning optical and electrochemical properties of Nb_2O_5 thin films via WO_3 doping, Trans. Electr. Electron. Mater. (2024), https://doi.org/10.1007/s42341-024-00572-x.
[116] S.H. Mujawar, A.I. Inamdar, C.A. Betty, R.C. Korošec, P.S. Patil, Electrochromism in composite WO_3–Nb_2O_5 thin films synthesized by spray pyrolysis technique, J. Appl. Electrochem. 41 (2011) 397–403, https://doi.org/10.1007/s10800-010-0249-9.
[117] D.M. Kabtamu, J.Y. Chen, Y.C. Chang, C.H. Wang, Electrocatalytic activity of Nb-doped hexagonal WO_3 nanowire-modified graphite felt as a positive electrode for vanadium redox flow batteries, J. Mater. Chem. A 4 (2016) 11472–11480, https://doi.org/10.1039/C6TA03936G.